fluids

MDPI

Review

Non-Spherical Cavitation Bubbles: A Review

Boxin Jia * and Hitoshi Soyama

Department of Finemechanics, Tohoku University, Sendai 980-8579, Japan; soyama@mm.mech.tohoku.ac.jp
* Correspondence: jia.boxin.q3@dc.tohoku.ac.jp; Tel.: +81-22-795-6899; Fax: +81-22-795-3758

Abstract: Cavitation is a phase-change phenomenon from the liquid to the gas phase due to an increased flow velocity. As it causes severe erosion and noise, it is harmful to hydraulic machinery such as pumps, valves, and screw propellers. However, it can be utilized for water treatment, in chemical reactors, and as a mechanical surface treatment, as radicals and impacts at the point of cavitation bubble collapse can be utilized. Mechanical surface treatment using cavitation impacts is called "cavitation peening". Cavitation peening causes less pollution because it uses water to treat the mechanical surface. In addition, cavitation peening improves on traditional methods in terms of fatigue strength and the working life of parts in the automobile, aerospace, and medical fields. As cavitation bubbles are utilized in cavitation peening, the study of cavitation bubbles has significant value in improving this new technique. To achieve this, many numerical analyses combined with field experiments have been carried out to measure the stress caused by bubble collapse and rebound, especially when collapse occurs near a solid boundary. Understanding the mechanics of bubble collapse can help to avoid unnecessary surface damage, enabling more accurate surface preparation, and improving the stability of cavitation peening. The present study introduces three cavitation bubble types: single, cloud, and vortex cavitation bubbles. In addition, the critical parameters, governing equations, and high-speed camera images of these three cavitation bubble types are introduced to support a broader understanding of the collapse mechanism and characteristics of cavitation bubbles. Then, the results of the numerical and experimental analyses of non-spherical cavitation bubbles are summarized.

Keywords: cavitation; cavitation bubble; cloud cavitation; vortex cavitation; numerical analysis; mechanical treatment

check for updates

Citation: Jia, B.; Soyama, H. Non-Spherical Cavitation Bubbles: A Review. *Fluids* **2024**, *9*, 249. https://doi.org/10.3390/fluids9110249

Academic Editors: Ashwin Vaidya and Rui Han

Received: 1 September 2024
Revised: 4 October 2024
Accepted: 16 October 2024
Published: 25 October 2024

Copyright: © 2024 by the authors. Licensee MDPI, Basel, Switzerland. This article is an open access article distributed under the terms and conditions of the Creative Commons Attribution (CC BY) license (https://creativecommons.org/licenses/by/4.0/).

1. Introduction

Bubbles are a normal phenomenon that can be observed in the fluid phase. According to Bernoulli's equation, decreasing static pressure until flow velocity reaches a specific value can create bubbles. This phenomenon of a phase change from the liquid phase to the gas phase is called "cavitation". Cavitation can even occur in animals in the natural world [1–9]. This phenomenon produces microjets that create plastic damage to a solid boundary [10,11]. Accordingly, this process causes erosion to hydraulic machinery, such as impellers, pumps, and pipes [12], but it can, nonetheless, be utilized in many fields. Cavitation can be used, for instance, in chemical reactors to promote oxidization in industrial processes. For example, the high pressures and temperatures caused by cavitation are proven to promote chemical reactions, and in this way, it can be applied in wastewater treatment as a type of advanced oxidation process [13,14], which is widely used today. In addition, cavitation can save energy and reduce costs compared to traditional processes [15–17]. Moreover, cavitation generated by ultrasound and hydrodynamics has also been used in microbial disinfection, biological wastewater treatment, and sonochemical reactors in biochemical engineering [18]. Elsewhere, in the case of biodiesel production, a hydrodynamic cavitation reactor was shown to be more effective and less costly than a traditional reactor [19–22]. Furthermore, cavitation reactors are highly effective at degrading specific contaminants in wastewater; for example, such harmful substances include industrial raw materials from manufacturing

plants, such as bisphenol [23]; a kind of antibiotic from stock raising, sulfamerazine [24]; a typical pollutant in wastewater, ammonia nitrogen [25]; fatty acids [26]; and algae (microcystis aeruginosa) [27]. Venturi-type [28], jet-type [29], swirling vortex-type [30], and rotor-type [31] reactors are widely used to create cavitation. When surface treatments with a cavitation impact are carried out by these devices, this is called "cavitation peening". This peening method uses cavitation impacts in the same way as shot peening, but a shot is not used in this method. Experiments have shown that it has advantages compared to traditional methods, as shown in Figure 1. One of its advantages is that the treated surface is smoother than that of traditional methods, such as shot peening [32]. Cavitation peening can be used, for instance, in automobile parts to extend their service life until failure [33–35]. However, as cavitation bubbles' collapse and rebound cause plastic deformation, it is essential that we develop an understanding of these bubbles' characteristics and properties if we are to avoid erosion.

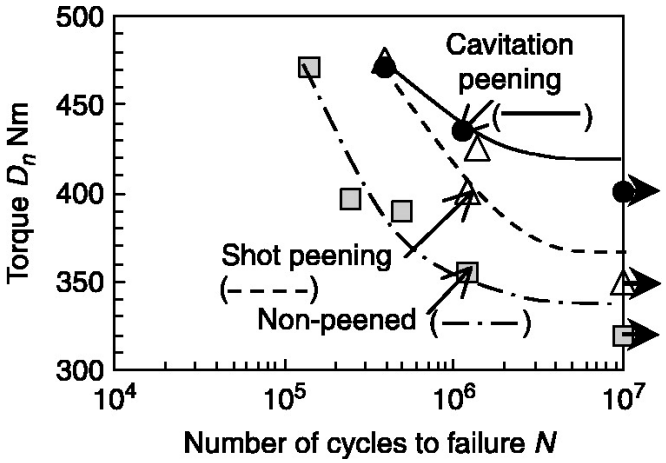


Figure 1. Improvement in the fatigue strength of the test gear via cavitation peening. Reprint from [35], with permission from Taylor and Francis, 2009, License Number 5803511487624.

In previous cavitation bubble research, Zhang et al. [36] comprehensively reviewed the interactions between cavitation bubbles and particles in silt-laden flows. Their work addressed the critical role of cavitation in hydraulic machinery and sediment transport, emphasizing the microscopic-scale interactions that contribute to material erosion and hydraulic efficiency. Such insights are invaluable for designing more durable hydraulic systems and understanding natural erosion processes. Further delving into the mechanics of cavitation, Wang and Chen [37] explored the thermodynamic behavior and energy transformation mechanisms during cavitation bubbles' collapse near rigid walls. Their numerical study elucidated how shock waves and jetting contribute to wall erosion and temperature changes, pinpointing the complex multi-phase flow dynamics. This work is pivotal for industries concerned with preventing cavitation-induced damage in fluid machinery and understanding the energy aspects of bubble collapse. Yu et al. [38] presented an innovative application of cavitation bubbles in fluorescence enhancement for bio-imaging. Through femtosecond laser-induced cavitation, they successfully amplified fluorescence signals in dye solutions without the drawbacks of nanoparticle use, such as biotoxicity and thermal damage. This advancement opens up new avenues for high-resolution imaging in biological research, where safe and effective fluorescence enhancement is crucial. On a practical front, Subramanian and Coutier-Delgosha [39] conducted intrusive experiments to better understand extreme conditions within collapsing cavitation bubbles. Reuter et al. [40] detected cavitation bubbles' dynamic impacts on a solid boundary by applying chronoamperometry. They found that the vortex ring created by collapsing bubbles has essential applications in deposition, mixing, and cleaning. Yasui [41] shed light on generating oxygen radicals from cavitation bubbles under ultrasound treatment, which expands our understanding of the chemical processes that occur within and around a collapsing bubble. The researchers

identified significant amounts of O radicals, alongside traditionally studied OH radicals, which opens up new avenues for exploring sonochemical reaction mechanisms and their potential applications. Ghasemian et al. [42] presented high-speed ultrasound imaging as a potent tool for non-invasively capturing the fast dynamics of single cavitation bubbles in tissue-mimicking material, highlighting the importance of advanced imaging techniques in observing these rapid phenomena. The review by Krell [43] on the degradation and protection of materials from cavitation erosion synthesized findings from various studies to assess the effectiveness of numerous protective treatments. Their review is critically important for understanding the relationships between material hardness, different treatment methods (such as plasma nitriding, shot peening, and coating deposition), and the improvement in or deterioration of resistance against cavitation erosion. Moreover, the dynamics of cavitation bubbles and their interaction with nearby solid boundaries were scrutinized in the research by Reuter et al. [44], which highlights the intricate flow fields and vortex dynamics associated with collapsing bubbles. The present investigation complements the detailed imaging studies already performed and provides a more robust theoretical framework for predicting and analyzing the impact forces and erosion mechanisms of cavitation on solid surfaces. Above all, we have taken an integrated approach to studying cavitation, which enriches the current scientific discourse and paves the way for future research and technological innovations around one of nature's most powerful and destructive phenomena.

Three types of cavitation bubbles will be introduced: single cavitation bubbles, cloud cavitation bubbles, and vortex cavitation bubbles. The stand-off distance (dimensionless distance) $\gamma = L/R_{max}$, where L is the distance between the center of the bubble and the wall surface, and R_{max} is the maximum bubble radius, is used to clarify the types of single bubbles [11,45,46]. Previous studies initiated research into cavitation bubble collapse, with the cavitation bubbles treated as spherical [47–49]. However, non-spherical bubbles occur in cavitation, especially when bubbles are in the final stages of collapsing [50–52]. With the development of visual techniques, it has been proven that these non-spherical bubbles are created in cavitation, as has been observed clearly in cavitation peening [28,29,53–55]. For example, bubbles are non-spherical in a type of cavitation peening termed laser peening (Figure 2) [56]. Furthermore, the X-ray images of the bubbles in vortex cavitation reveal that they are angulated [55], not spherical or spherical-like, as previous numerical analyses indicated. Today, to close the gap between numerical analyses and field experiments, it is of significant value to research non-spherical bubbles in cavitation peening.

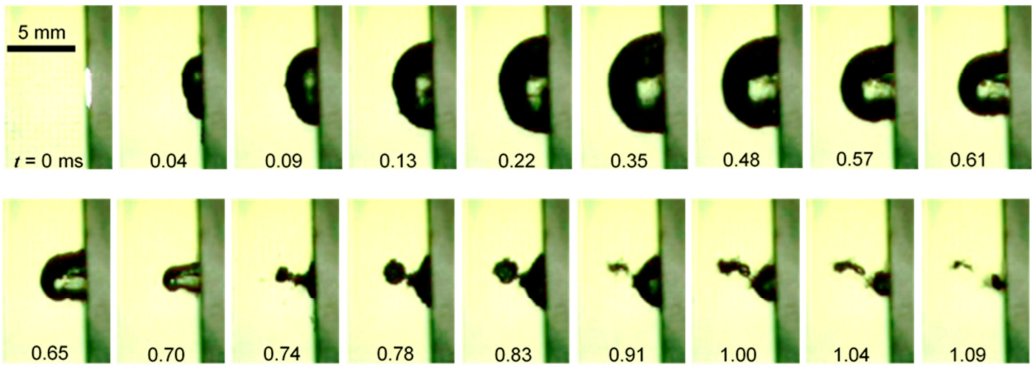


Figure 2. Images of laser cavitation on the wall near the glass chamber [56].

Returning to the initial study of bubbles, Figure 3 depicts the collapse of a solid cavitation bubble near a boundary in water [49]. As this shows, the bubble becomes non-spherical as it collapses and finally disappears. Roles are played in this process by stress and pressure. In this review, based on numerical analyses and field experiments, we explain the change in bubble shape and introduce the volume of pressure released near the solid boundary during that process, applying these ideas to scenarios from a single non-spherical cavitation bubble to complicated gathering bubbles. For complicated gathering bubbles, such as in cloud cavitation and vortex cavitation, more accurate simulations are

presented than those in previous work, wherein we consider that these two cavitation processes involve non-spherical bubbles. Above all, this review emphasizes that the impact of bubbles collapsing near a solid wall is deeply related to the shapes of the bubbles in question.

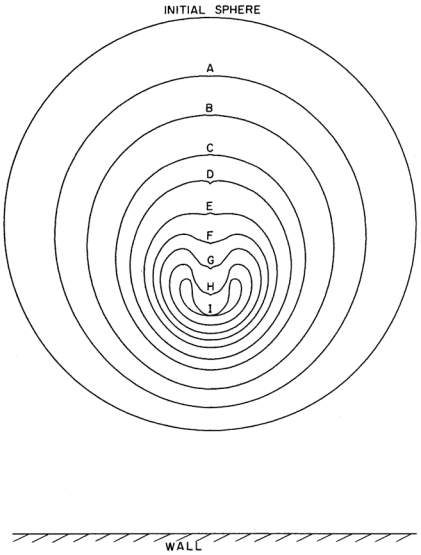


Figure 3. Collapse of a solid cavitation bubble near a boundary in water, computed by Plesset and Chapman. A–I represent different shapes as time goes on. Reprint from [49], with permission from Cambridge University Press, 1971, License Number 5724030138904.

In sum, this review describes and discusses non-spherical cavitation bubbles to help readers understand cavitation and its applications [57–59]. This review also discusses the relationship between single cavitation bubbles and complicated cavitation, such as the cases of cloud cavitation and vortex cavitation.

2. Single Cavitation Bubbles

This section will review research on single spherical and non-spherical cavitation bubbles. Figures 4 and 5 clearly show a cavitation bubble near a solid boundary, as published in early research [11,48]. When this research field first formed, investigations sought to find numerical solutions for the collapse and rebound of a spherical bubble in water [12]. They focused on the effect of liquid compressibility, and a numerical solution was obtained through a simple gas-like model. The calculations of the motion of the bubble wall and the gross effect of the gas content of the bubble are shown in Figure 6 (based on the irrotational assumption because the motion is spherically symmetric) [47]. In this figure, U is the velocity of the bubble's center, and c is the velocity of the sound in liquid. γ explains the gross behavior of the gas, while $\gamma > 1$ indicates that some of the heat of compression is retained in the gas.

Although this numerical analysis focused on spherical bubbles, it established crucial groundwork for us to gain an understanding of bubble collapse and rebound mechanics. Chiefly, it proved that the formation of cavitation bubbles damages a solid surface, which arises from pressure waves that originate from the bubbles. This understanding can be extended to the analysis of non-spherical cases.

Continuing this trajectory, a new wave of numerical analysis of spherical bubble collapse near a solid boundary has been introduced [49]. Here, the simulation is based on small steps used to calculate the velocity of the movement of the bubble surface. Since flow occurs via irritation, and viscosity and compressibility are neglected, the calculation is based on cylindrical coordinates. The finite difference method is applied to assess the interaction of a collapsing bubble with a solid surface, which is also the process through which spherical bubbles become non-spherical, as shown in Figure 3. This field of study

critically discusses non-spherical bubbles and explains the "water hammer", highlighting the complexities introduced by the boundary condition, which may affect the symmetry of collapse and potentially lead to asymmetric or non-spherical bubble shapes. This sets the stage for the numerical analyses of bubbles collapsing that lack spherical symmetry.

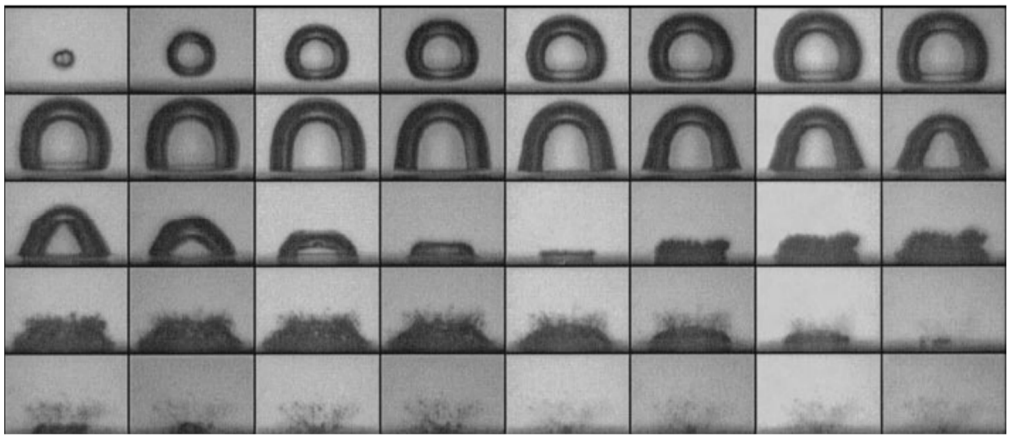


Figure 4. Cavitation bubble dynamics in the vicinity of a solid boundary. Reprint from [11], with permission from Cambridge University Press, 1998, License Number 5831440015629.

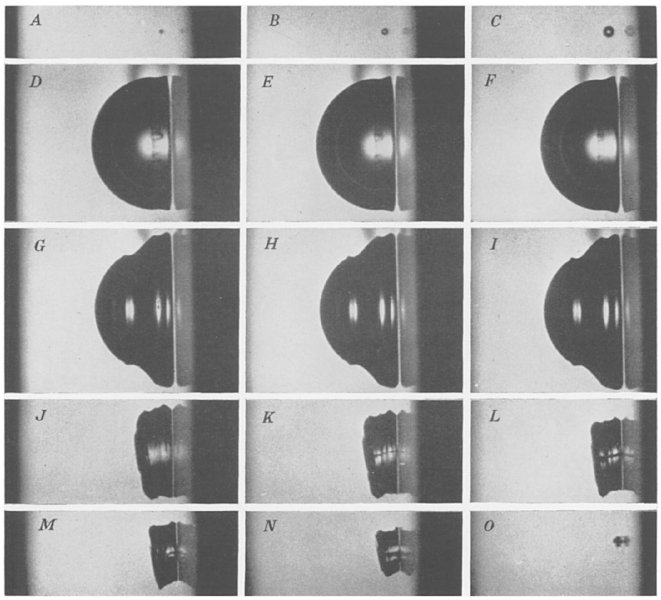


Figure 5. Growth of cavity from nucleus very close to a solid wall, and subsequent collapse. Timing: (**A**–**C**) at 0, 0.2, and 0.4; (**D**–**F**) at 5.8, 6.0, and 6.2; (**G**–**I**) at 11.4, 11.6, and 11.8; (**J**–**O**) at 16.8 to 17.8 ms. Reprint from [48], with permission from Royal Society (Great Britain), 1966, License Number 1492359-1.

To further research the bubble-collapsing effect, the dynamics of the shock-induced collapse and Rayleigh collapse of a bubble near a planar rigid surface and in a free field have been numerically analyzed [52]. This research has charted the whole process of bubble collapse, from the unsteady Euler equation used for calculations to the bubble's properties. Bubble collapse has been divided into two parts: free-field shock-induced collapse and Rayleigh collapse. Importantly, Rayleigh collapse is not spherically symmetric, meaning it applies to non-spherical bubbles. Shockwave collapse, including the precursor, water hammer, and pressure released, is demonstrated in Figure 7. The wall pressures of these two types of collapse have also been calculated. Through these numerical analyses, researchers have gained a greater understanding of bubble dynamics for both theoretical

frameworks and practical applications, showing bubble behavior influences the system performance and material integrity.

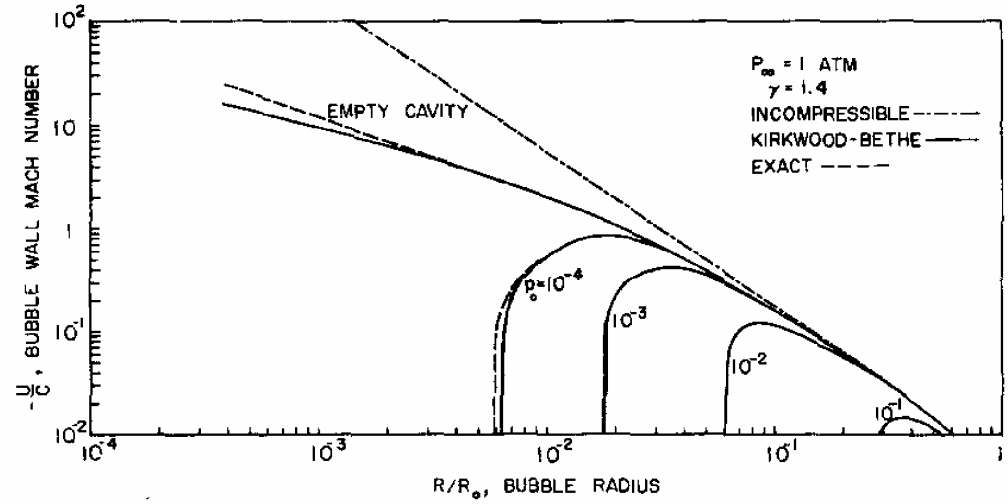


Figure 6. The bubble–wall Mach number as a function of the bubble radius with a decreasing gas content. The gas content is determined by its initial pressure p_0 in atmospheres. The index γ has the value 1.4, and the ambient pressure p_∞ is 1 atm. Reprint from [47], with permission from AIP Publishing, 1964, License Number 5806350103845.

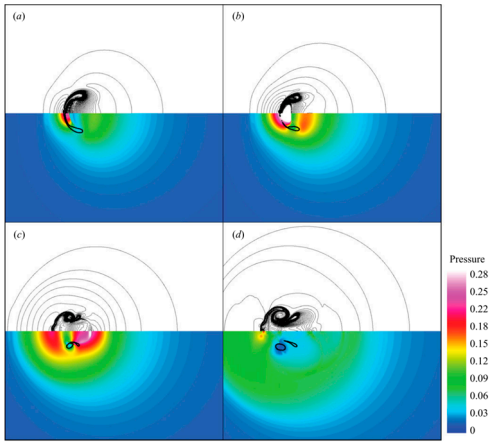


Figure 7. Water hammer shock in free-field shock-induced collapse (p_s/p_o = 353) at times (**a**) $t/(R_o/c_L)$ = 8.49, (**b**) $t/(R_o/c_L)$ == 8.68, (**c**) $t/(R_o/c_L)$ == 9.05, (**d**) $t/(R_o/c_L)$ == 9.52. Top: density lines; bottom: pressure contours non-dimensionalized by $\rho_L c_L^2$ (approximate interface location: γ = 1.42 contour). p_s: The shock pressure; p_o: The relevant pressure ahead of the compression; R_o: The radius of bubble; ρ_L: The ambient density of the water; c_L: The sound speed of the water. Reprint from [52], with permission from Cambridge University Press, 2009, License Number 5830760763951.

Numerical analyses and experimental observations have since been introduced that focus on the impact between the front of the re-entrant jet and the opposite side of the bubble, with the jet penetrating the slower-moving liquid close to the rigid boundary, which is called the "final stage of the bubble collapsing to a rigid boundary" [50]. The experimental research on this topic uses high-speed photography, with up to 5 million images per second. An incompressible impact model has enabled the comprehensive numerical analyses of bubble–boundary interaction mechanisms. The photographs of bubbles collapsing and the corresponding numerical analyses are shown in Figure 8. The evolution of the velocity field and pressure contours in the toroidal stage of bubble collapse for 1.1 is shown in Figure 9. This research has observed a transformation of kinetic energy from the radial flow into the main bubble to a rotational flow around the cavity next to the

wall during the final stage of a bubble collapsing, and this transformation has ensured a "boundary" $\gamma = 1$. When $\gamma < 1$, the shock wave emission has weakened, which causes a reduction in the damage to the wall. This field of study is pivotal in identifying bubble interaction during cavitation events.

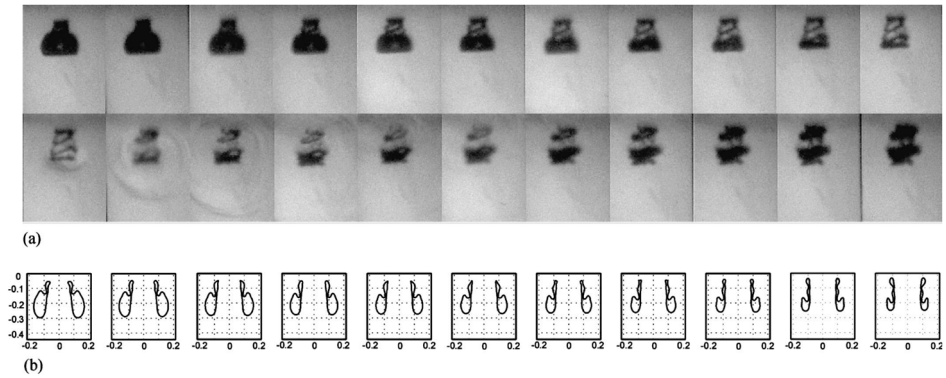


Figure 8. The final stage of the collapse of a cavitation bubble for $\gamma = 1.1$. (**a**) High-speed photographic record of bubble motion; frame interval 200 ns, frame width 1.4 mm. The location of the rigid boundary is at the upper limit of the frames. (**b**) Computed bubble profiles covering the time interval correspond to the photographic record's first row. The nondimensional times are t = 2.0084, 2.0097, 2.011, 2.0123, 2.0136, 2.0149, 2.0161, 2.0174, 2.0187, 2.02, and 2.0213. Reprint from [50], with permission from AIP Publishing, 2002, License Number 5806350497331.

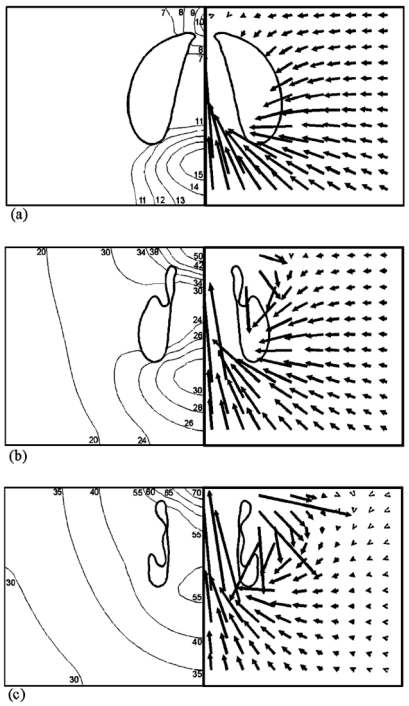


Figure 9. Evolution of the velocity field (**right**) and pressure contours (**left**) for the toroidal stage of bubble collapse for γ = 1.1. The letters correspond to the following nondimensional times: (**a**) 1.9981, (**b**) 2.011, and (**c**) 2.0213. Reprint from [50], with permission from AIP Publishing, 2002, License Number 5806350497331.

Research on single cavitation bubbles has practical implications for reducing material erosion caused by cavitation. The effect of liquid droplet impingement (LDI) on a material surface has been thoroughly researched [60]. Using the model of droplet capture at a gas–liquid interface, the fluid pressure on the material surface and the normal stress in the vertical direction of that material surface have been calculated. A simulation of the pressure

in a fluid and the equivalent stress in a material on a wet surface is shown in Figure 10. Compared to the same situation on a dry surface, the simulations reveal a significant finding—the impinged droplet pressure decreases, which can diminish the equivalent stress inside the material. This damping effect can be attributed to the liquid film's ability to absorb and disperse the energy imparted by the impinging droplet, culminating in a reduced impact force. Furthermore, the research has led to the development of an empirical formula that quantifies the damping effect, relying on the critical fluid factors of LDI. This research provides an insightful analysis of the damping effects of a liquid film on a material when subjected to high-speed LDI. Its model allows for predicting and optimizing the responses of various materials to LDI scenarios, potentially leading to enhanced erosion resistance in fluid systems. It is also essential in such work to note the effect caused by bubbles collapsing, which should inspire further research and development in this field.

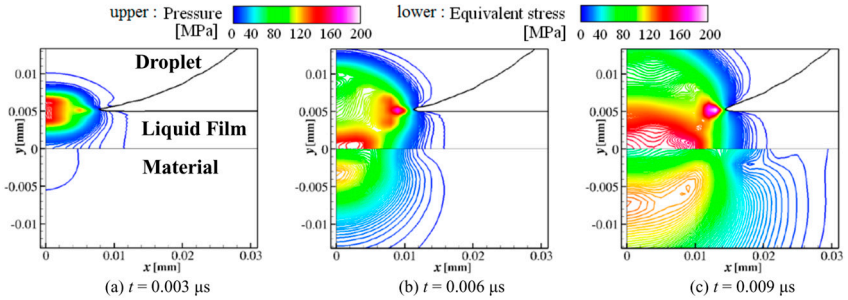


Figure 10. Time variation in pressure in fluid and equivalent stress in material on wet surface. Reprint from [60], with permission from J-stage, 2016.

The relationship between a non-spherical bubble collapse and the stress state of the nearby boundary/wall [45] has been examined to ascertain how varying distances between the bubble and the wall, called the stand-off distance (as mentioned before, γ), impact material stress. The mathematical model is shown in Figure 11, which corresponds to one-quarter of a three-dimensional space. Here, R_0 is the bubble radius and L is the distance between the bubble center and the wall. The governing equation used is similar to [60]. By conducting coupled fluid–material numerical simulations, studies have revealed that different collapse modes—pancake-shaped, hemispherical, microjet, and detaching modes—affect the stress distribution within adjacent materials. Some of the calculated results are shown in Figure 12. Furthermore, the relationship between the stand-off distance and the maximum equivalent stress is shown in Figure 13. The result is calculated by a supercomputer, and the CFD (computational fluid dynamics) code is Fortran in the Linux system. The calculation time for one stand-off distance is about 60 h. These figures provide a complete numerical analysis of the first stage of non-spherical bubble collapse. The peak of equivalent stress on the material surface can be observed when the stand-off distance is 0.3–1.0. This area of study underscores the complexity of bubble–material interactions and the potential for significant material damage, highlighting the importance of understanding these dynamics for protective material design and fluid system maintenance.

Further expanding on bubble interactions, Aganin et al. [61] introduces a particle model to simulate the behavior of weakly non-spherical bubbles. The model provided in that research focuses on the bubble's interaction. Unlike typical research, compressibility effects and the liquid viscosity effect are considered. Applying this model, a bubble collapsing near a solid boundary was simulated, along with the simultaneous interaction of three bubbles, as shown in Figures 14 and 15. This research has been instrumental in progressing the field of study from individual bubble dynamics to the interactions between multiple bubbles, which is crucial in many practical scenarios where bubble populations rather than isolated bubbles influence the system's overall behavior. Furthermore, the model accurately shows the relationship between the stand-off distance and stress caused by a bubble collapsing. One finding is that if the distance between the bubbles is smaller, this will produce a better result in the simulation. Above all, the particle model approach

allows for more sophisticated simulations of bubble interactions, offering insights into the collective dynamics of bubble populations under various conditions, and the model has been proven to have a goodness of fit in the simulations of bubble collapse.

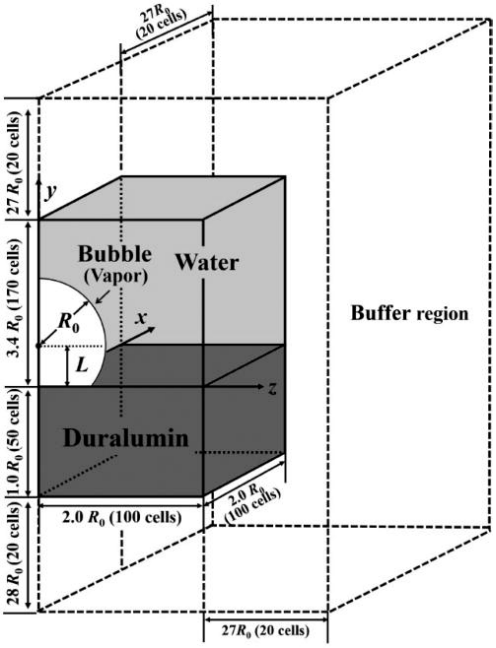


Figure 11. The mathematical model of the non-spherical bubble [45].

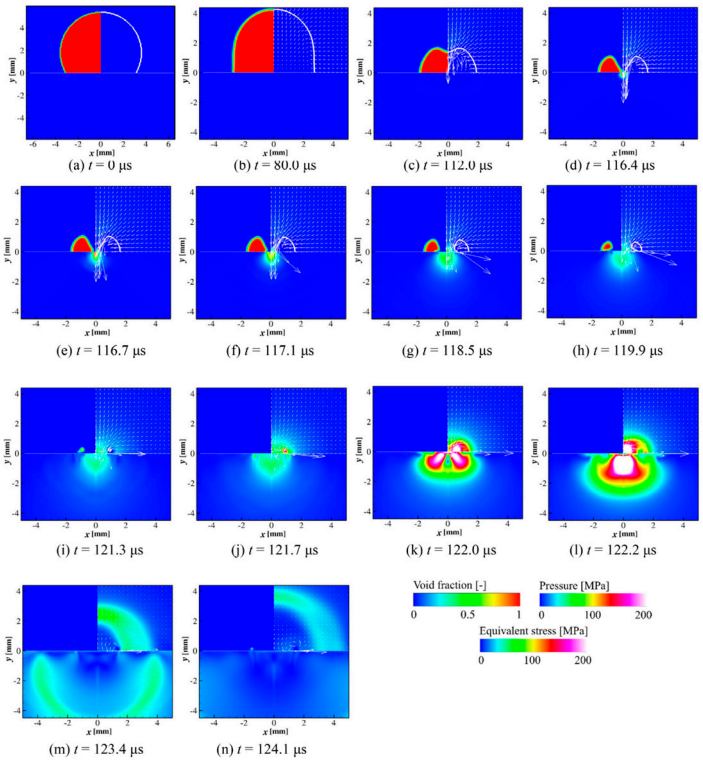
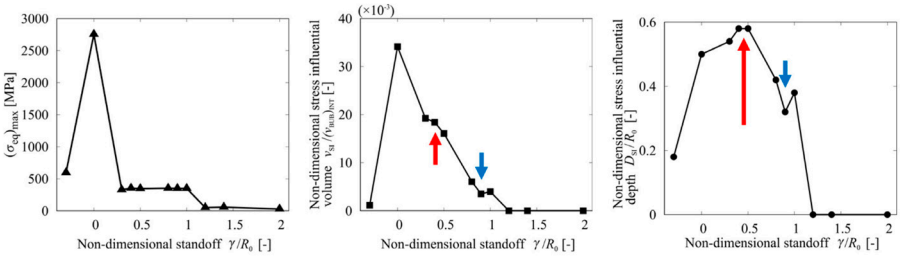


Figure 12. Time evolution of the void fraction (**upper left** of each sub-figure), pressure, and velocity vectors (**upper right**) in the fluid domain, and equivalent stress in the material domain (**lower**) ($\gamma = 0.5$) [45].



(a) Maximum equivalent stress (b) Volume of stress influential area (c) Depth of stress influential area

Figure 13. Variation in maximum equivalent stress and stress influence area with the stand-off distance between the bubble and the wall. The blue and red arrows point γ/R_0 = 1 and 0.5. [45].

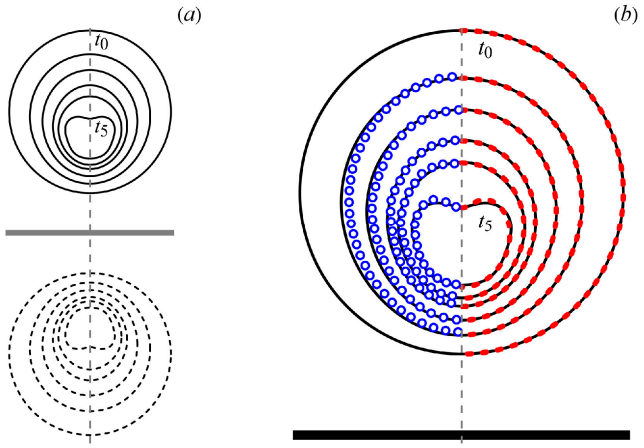


Figure 14. Evolution of the axial section of a bubble collapsing near a plane wall (t_0 corresponds to the beginning of collapse): (**a**) the results of a simulation of the interaction between two bubbles by the proposed model (solid lines correspond to the bubble under consideration; dashed lines present its mirror image), and (**b**) the same results for the bubble considered (solid lines), along with experimental data and the results obtained by the boundary element method (dashed lines). Reprint from [61], with permission from Elsevier, 2024, License Number 5830790844530.

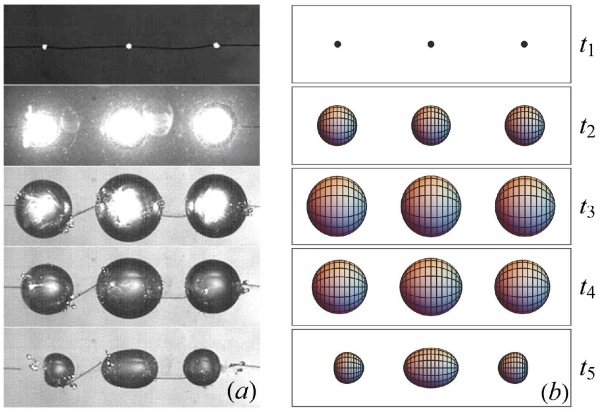


Figure 15. Interaction between three bubbles simultaneously produced collinearly at nearly equal inter-bubble distances: (**a**) in the experiments by Cui et al., and (**b**) in the simulation by the present model. Reprint from [61], with permission from Elsevier, 2024, License Number 5830790844530.

These studies have contributed significantly to broadening our understanding of cavitation bubbles, including spherical and non-spherical bubble dynamics in fluid systems. However, most research on non-spherical bubbles has a central issue—uncertainty around the erosion of the material surface caused by the bubble collapsing. To address that, many numerical analyses and experiments have been performed, seeking to explain the

interaction and relationship between a bubble collapsing and a solid boundary. The progression from single-bubble dynamics to complex interactions between bubbles and with materials underlines the evolving landscape of bubble research, paving the way for further explorations and innovation in bubble behavior modeling and its application to material processing and fluid mechanics.

3. Cloud Cavitation

The exploration of bubble cloud dynamics, especially near rigid boundaries, in non-spherical bubble research has formed an active area of fluid dynamics study given the physical applications for the research findings, including those relating to cavitation peening. In this section, we introduce several studies on bubble clouds involving complex physical phenomena, such as shock wave emission, jet formation, and pressure fluctuation, which significantly impact the efficiency and effectiveness of cavitation bubble processes.

Building upon the foundation of single-bubble dynamics, Chahine and Duraiswami [62] expanded the investigation to multiple bubbles, presenting a study on the dynamic interactions in multi-bubble clouds. Their methodology combined analytical techniques and numerical simulations to capture the complex dynamics of bubble–bubble interactions within a cloud. Significantly, they found an agreement between the two approaches within their studied range, highlighting the role of bubble–bubble interactions in determining the collective behavior of bubble clouds. Their work is crucial for understanding the mesoscale dynamics within these clouds, which bridge the gap between individual bubble behavior and the macroscopic flow characteristics.

An early contribution to understanding the bubble cloud dynamics near a rigid boundary came in the form of experimental and numerical investigations of the final stage of the collapse of a cavitation bubble close to a rigid boundary [63]. This research offers invaluable insights into the behavior of liquid jets developed during bubble collapse and the shock wave emissions corresponding to the "splash" effect, as determined by employing high-speed photography alongside numerical simulations. Here, the wave emission caused by bubble clouds was researched to explain the mechanism of adverse effects. The study introduced the "cloud interaction" parameter to describe cloud bubbles in numerical analyses:

$$\beta = \alpha_0(1-\alpha_0)A_0^2/R_0^2 \quad (1)$$

where the initial radius and void fraction of the cloud are denoted by A_0 and α_0, respectively, and the initial radius of the bubbles within the cloud is denoted by R_0. The cloud bubbles can be divided into several steps: traveling bubble cavitation, maximum cavity length, re-entrant jet, bubbly mixture, local pulse phenomena, and global pulse phenomena. Figure 16 shows the global pulse phenomena created by the shock wave released. The findings shed light on cavitation erosion mechanisms, linking the bubble–boundary interaction with potential damage risks in hydraulic machinery and other fields.

Experimental measurements using a high-speed camera have shown that the bubble cloud damages the material surface, which was ascertained by detecting the occurrence of impulse pressure during the incubation of the bubble. The reason for the impulse pressure is that various distinct cavitation structures arise from the mixture of bubbles. However, the experiment highly depends on the beta parameter, which decides the size of a bubble cloud. Here, a large bubble cloud seems suitable for the numerical analysis model. This research has identified important features of fluid flows and explained the mechanism of impulsive pressure caused by bubble clouds.

The exploration of bubble cloud dynamics close to rigid boundaries was furthered in [51]. In this investigation, the researchers meticulously documented the final collapse stage of a bubble cloud near a rigid boundary, providing critical insights into the complex interactions that occur as a bubble cloud collapses. By using ultra-high-speed photography, which can produce precise images, the researchers observed two secondary shock wave emission types during cloud rebound, as shown in Figure 17. The first type, secondary shock wave emission, is a consequence of the free collapse of a bubble within the cloud as a

result of the ambient pressure in the fluid. The second type of shock wave emission is due to the interaction of the cloud collapse-induced shock wave with microbubbles close to the cloud's collapse site. In the study, it seems that no jet formation was observed during the process of the cloud bubble collapsing. In this scenario, the single bubbles are probably too small to induce the formation of liquid jets. The study highlights the influence of rigid boundaries on the collapse process, presenting a detailed analysis of the pressure fields and mechanical effects involved, which can aid future research work to find a method for reducing collateral damage.

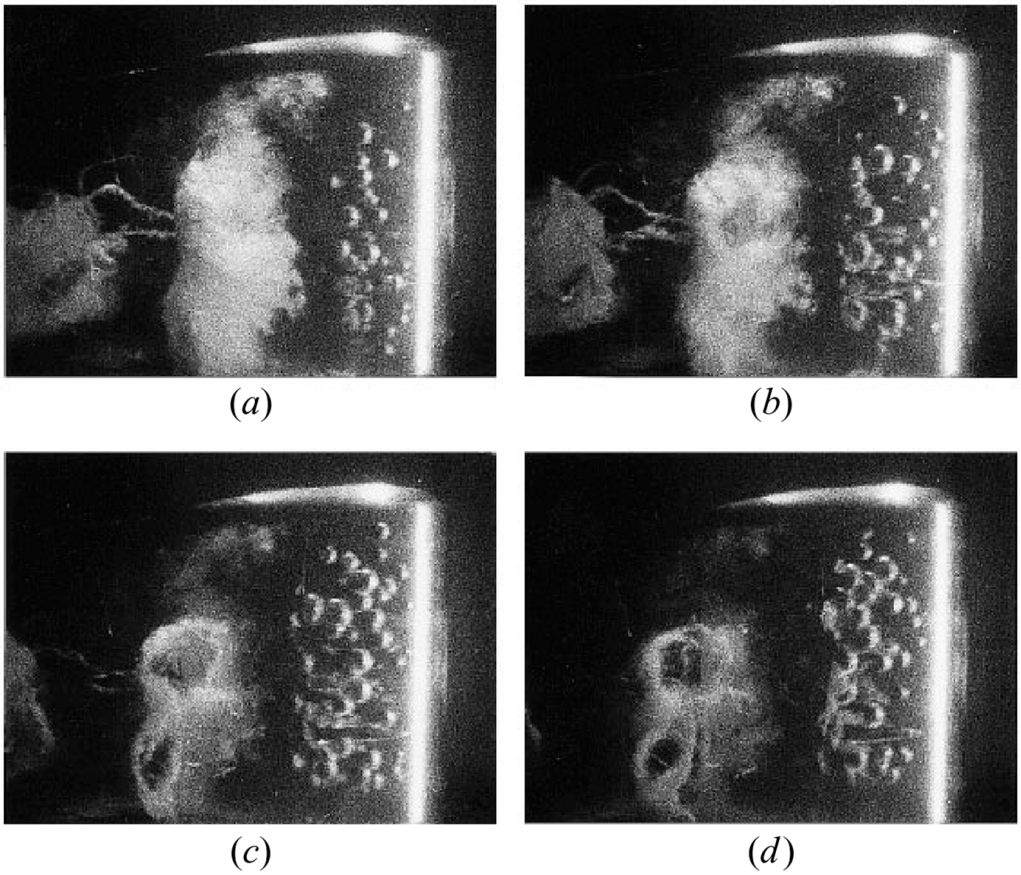


Figure 16. Consecutive high-speed movie frames (2 ms apart) showing global cloud collapse. (**a**–**d**) depict four consecutive frames from one such movie. Reprint from [63], with permission from Cambridge University Press, 1998, License Number 5830810037327.

Expanding the numerical methods available to explore bubble dynamics, a significant contribution arose with the development of a two-way coupled Eulerian–Lagrangian model that elucidates the microbubble cloud dynamics, accounting for incoming pressure waves and the resultant pressure loads on nearby rigid walls [64].

To simulate the two-phase medium as a continuum and solve the N-S equations, two models are introduced: a continuum homogeneous mixture flow model and a bubble motion and volume change model. According to the homogeneous mixture flow model, the mixture density is defined as follows:

$$\rho_m = (1 - \alpha)\rho_l + \alpha\rho_g \quad (2)$$

where the subscripts "l" and "g" represent liquid and gas properties, respectively, while is the gas volume fraction.

The governing equation for bubble motion and volume change takes the form of a modified Rayleigh–Plesset–Keller–Herring equation:

$$\left(1-\frac{\dot{R}}{c_m}\right)R\ddot{R}+\frac{3}{2}\left(1-\frac{\dot{R}}{3c_m}\right)\dot{R} = \frac{\left(u_{enc}-u_b\right)^2}{4}+\frac{1}{\rho_m}\left(1+\frac{\dot{R}}{c_m}+\frac{R}{c_m}\frac{d}{dt}\right)\left[p_v+p_g-p_{enc}-\frac{2\gamma}{R}-4\mu_m\frac{\dot{R}}{R}\right] \quad (3)$$

In the above, c_m is the local sound speed in the mixture where the bubble is located, μ_m is the medium viscosity, p_v is the liquid vapor pressure, p_g is the initial gas pressure in the bubble, k is the gas polytropic constant, γ is the surface tension, and u_b is the bubble center velocity. A pressure term is added, $(u_{enc}-u_b)^2/4$, due to the bubble slip velocity relative to the liquid, and the surface-averaged pressure (SAP) model is used to determine the encountered liquid quantities. p_{enc} and u_{enc} are the encountered pressures and velocities, respectively, in the liquid averaged over the bubble surface. This averaging procedure accounts for non-uniform pressures and velocities along the bubble surface. Using p_{enc} results in a significant improvement over classical models, which use the pressure at the bubble center. Calculation results for bubble locations and pressures can be obtained from this equation.

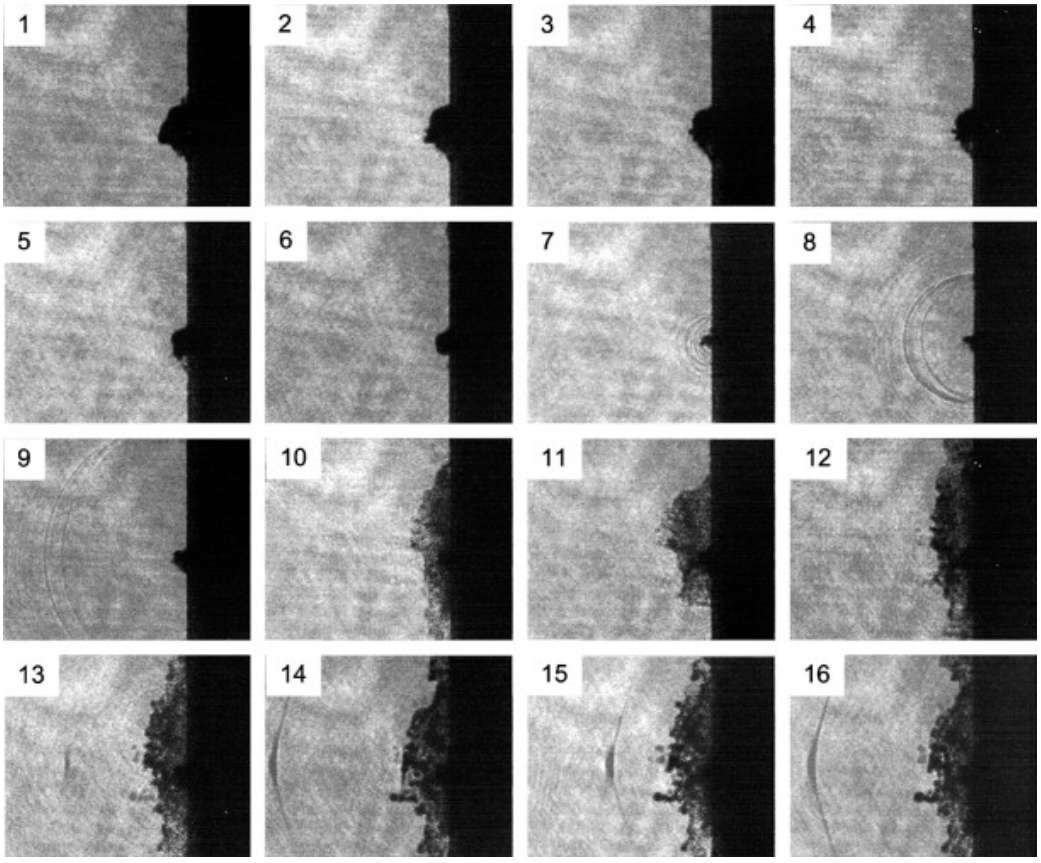


Figure 17. Collapse phase of a hemispherical bubble cloud. Frame interval 500 ns. The first frame was taken 159.55 µs after the application of ultrasound. Frame width 2.56 mm. The collapse point of the cloud occurs between frames 7 and 8. The main shock wave emission during cloud rebound can be seen in frames 8 and 9. Reprint from [51], with permission from Elsevier, 2011, License Number 5830811192279.

Moreover, the field of study of the dynamics of a bubble cloud near a rigid wall extends our comprehension of how external pressure frequencies and amplitudes influence bubble behavior and the subsequent pressures exerted on adjacent surfaces [65]. Furthermore, this

research identifies resonance frequencies that significantly differ from natural frequencies, which exemplifies the complexity of bubble dynamics, particularly in terms of nonlinear effects and the generation of high pressures at the contacting walls. Figure 18 shows bubble radii versus time for different bubbles in the cloud and the corresponding pressure variations. As the resonance frequency, a pressure peak order of magnitudes higher than the excitation pressure occurs, which corresponds to a match between the driving pressure reaching its maximum and the collective individual bubbles collapsing.

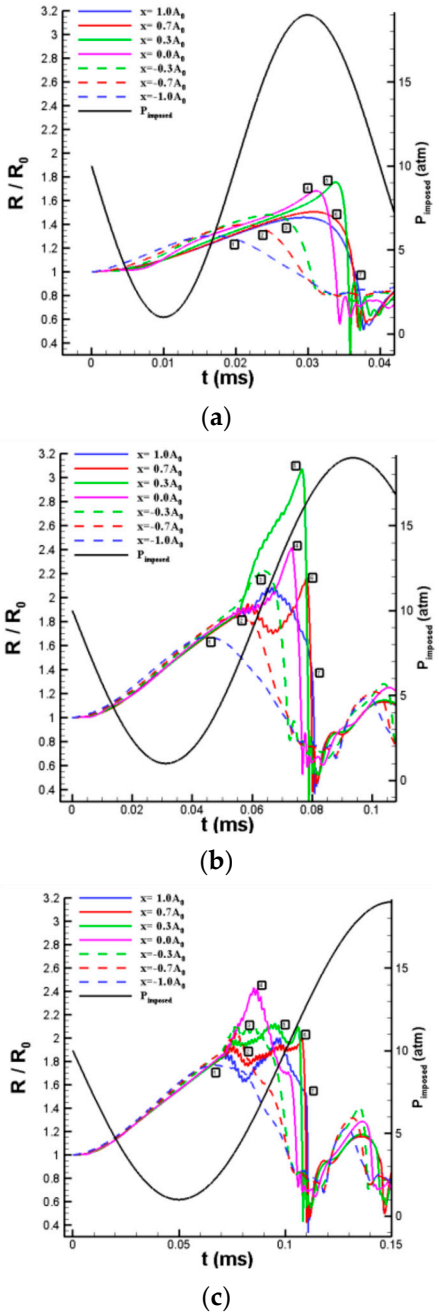


Figure 18. Comparison of bubble radii at different cloud locations for a bubble cloud excited at different pressure frequencies: (**a**) f = 25 kHz; (**b**) f = 8 kHz, and (**c**) f = 5 kHz [65].

Such modeling efforts highlight the critical role of the driving pressure's frequency in determining bubble cloud dynamics, which allows for distinguishing between collective cluster behavior and non-synchronized oscillations based on resonance conditions. Building upon this empirical groundwork, the authors of [66] present simulation-based insights into

acoustically driven bubble cloud dynamics near a rigid wall. The numerical study provides a comprehensive view of how acoustic pressures influence bubble behavior, detailing bubble clouds' formation, growth, and collapse near rigid surfaces. In addition, the impacts of the amplitude and frequency of the excitation pressure, the cloud and bubble sizes, the void fraction, and the initial stand-off distance on the bubbles are all discussed and subject to numerical analysis. The researchers' mathematical model of cloud bubbles is shown in Figure 19, where R_0 is the radius of a single bubble, A_0 is the radius of the cloud, and X_0 is the distance between the solid boundary and the center of the cloud. Their analysis also produced important findings on cloud bubble distributions and internal pressures, as shown in Figure 20.

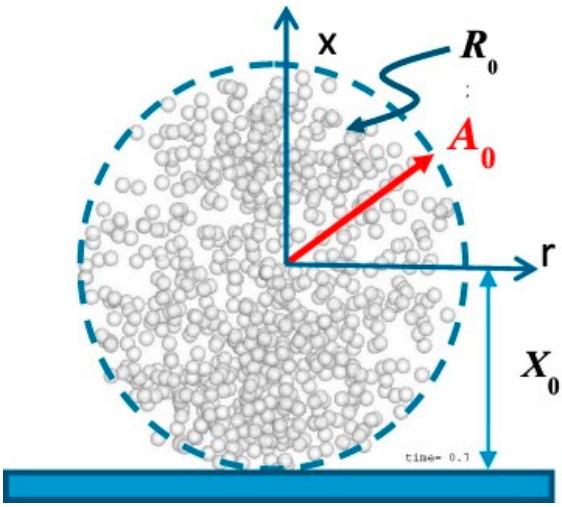


Figure 19. The mathematical model of cloud bubbles [66], with permission from Elsevier, 2018, License Number 5880601502087.

An experimental perspective was provided through a focused study on bubble–sphere interactions near a rigid wall [53], which delved into the varying degrees of interaction between oscillating bubbles and movable spheres. The research categorized the interactions into weak, intermediate, and firm based on distinct bubble shapes at the maximum volume, offering a classification that underlines the significance of bubble–sphere dynamics in the broader context of bubble behavior near rigid boundaries. The intense interaction between the bubble and sphere near a rigid boundary is shown in Figure 21.

Utilizing the Euler–Lagrange method we have mentioned, a new numerical simulation was performed of a solid's stress due to a bubble cloud's collapse [67]. The bubble radius and void fraction distribution for various stand-off distances are shown in Figure 22. The study discovered that the critical point of the stand-off distance $Y_C = 0.4R_c$. At this point, the von Mises stress has the highest value, and then it decreases. This research team's models may become more accurate in the future when considering mass transfer, but the published work to date gives a clear indication of the direction they are taking in developing their numerical analysis.

The early-stage dynamics have been investigated of hydrodynamic cloud cavitation, focusing on bubble size distribution (BSD) [68]. The novel application of a fiber optic probe to assess the BSD within a cavitation cloud sheds light on the significant role of turbulence in bubble fragmentation processes. The cloud cavitation in four successive shedding cycles is shown in Figure 23, taken from another literature work [69]. This study identifies two distinct power-law scales corresponding to different stages of bubble development, thereby improving our understanding of the mechanisms driving bubble formation and breakup in cavitation clouds. This research direction is instrumental in elucidating the microscale processes that precede the macroscopic phenomena observed in cavitation erosion and noise generation.

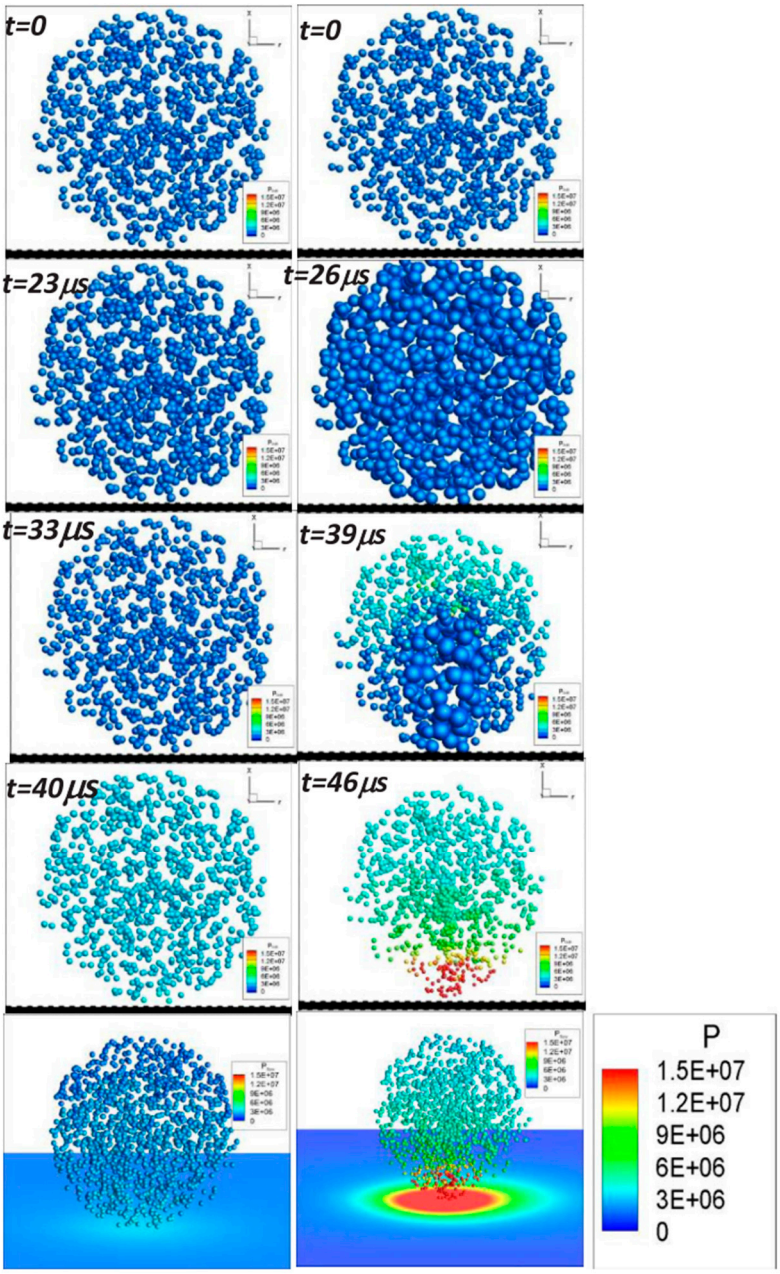


Figure 20. Time sequence of bubble distributions and internal pressures (indicated by the colored contours) in a bubble cloud driven by pressure excitation with two amplitudes. The last frame of each row is a view of the pressures at the rigid wall [66], with permission from Elsevier, 2018, License Number 5880601502087.

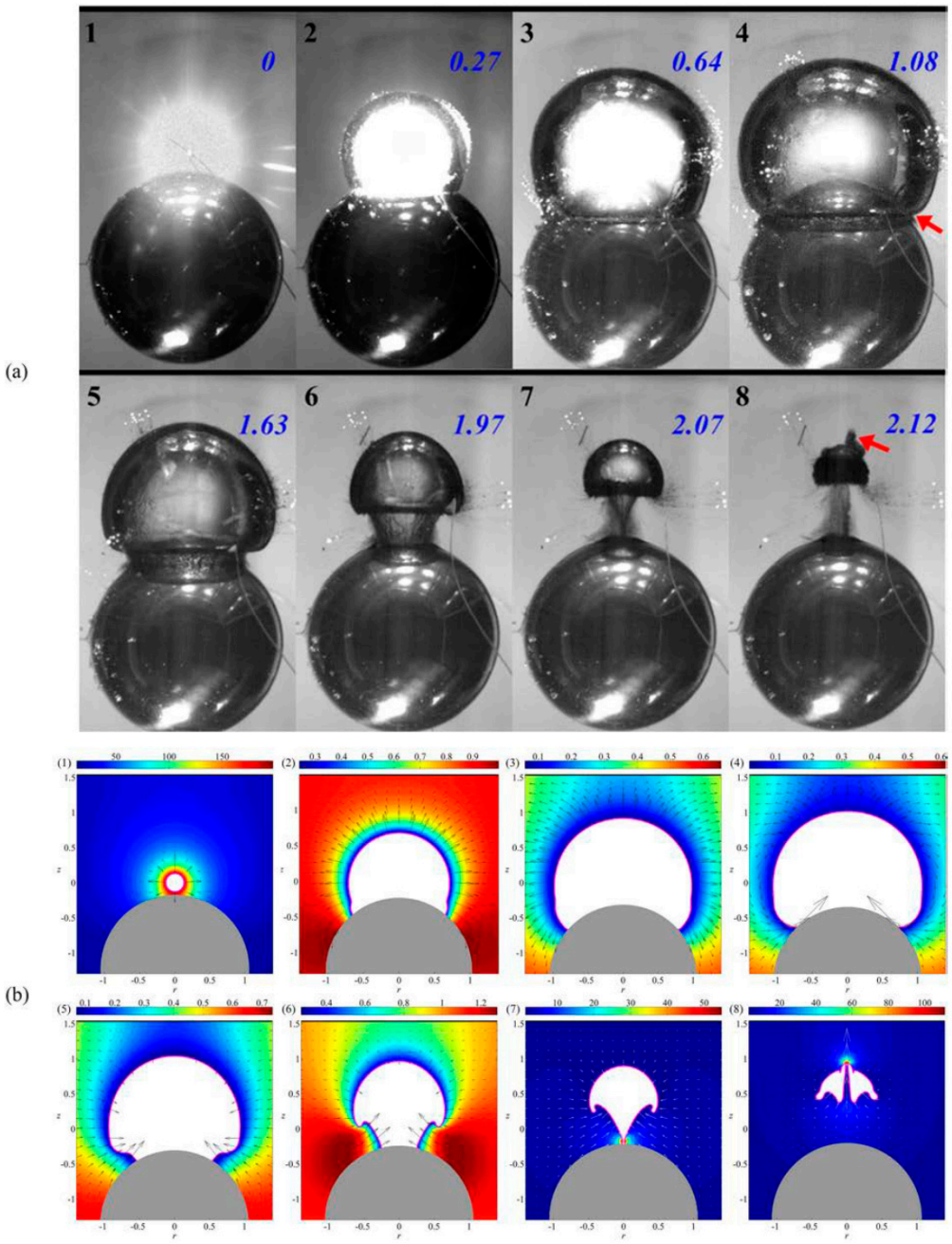


Figure 21. Strong interaction between the bubble and sphere near a rigid boundary. (**a**) Experimental images. Frames 1–9 depict the first cycle of the bubble and it is noted that the bubble bottom gains a higher local curvature (frames 4–6) due to the retardation effect from the sphere. An upward jet forms at the bubble bottom afterwards, and a strong spray at the jet tip can be observed in frame 7, leading to the unstable bubble surface after the jet impact. Frames 10–14 depict the second cycle of the bubble. The bubble migrates towards the wall during the rebounding phase and collapses onto the wall directly in the recollapse phase (frames 13 and 14). (**b**) Numerical results. The jet tip assumes a mushroom shape, which has favorable agreement with the experiment. Reprint from [53], with permission from AIP Publishing, 2017, License Number 5830821246785.

There has also been further exploration of the intricacies of bubble dynamics, clouds' internal structures, and their formation mechanism within cloud cavitating flows [70]. This study, centered on numerical investigations, elucidated the complex internal arrangements of bubbles within a cavitating cloud, mainly focusing on the mechanisms driving these formations. While the inquiry prioritized cloud cavitation, the insights gleaned have sub-

stantial relevance for understanding bubble dynamics near rigid boundaries since they shed light on the bubble cloud's structural evolution and interactions with surrounding flows, as shown in Figures 24 and 25. Such insights are valuable for refining bubble dynamics models, especially for use in predicting and mitigating the effects of cavitation in engineering systems and enhancing the efficacy of therapeutic applications involving ultrasound.

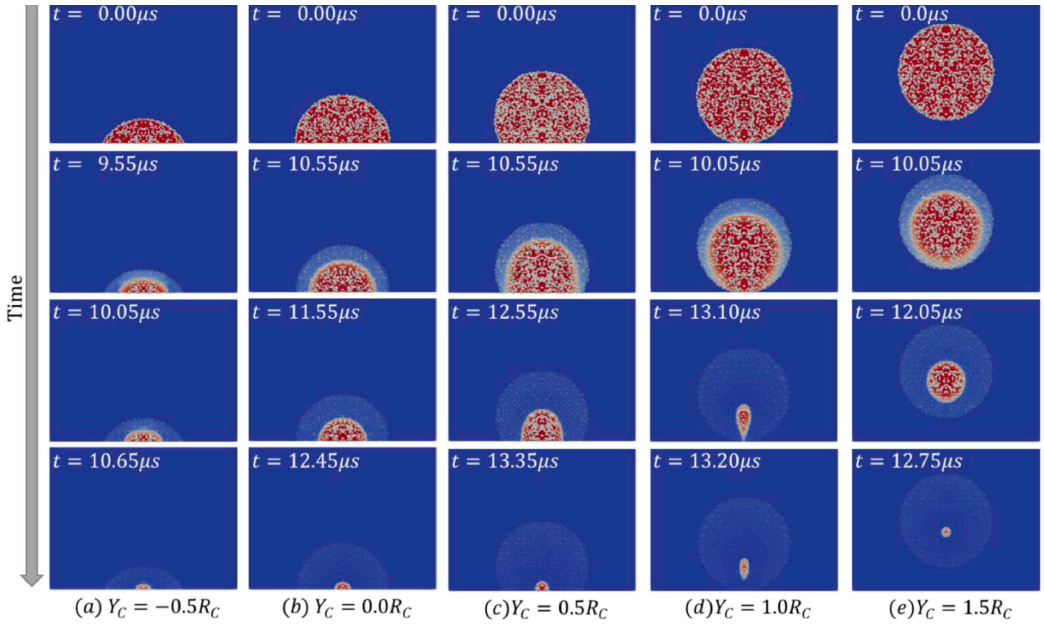


Figure 22. Time evolution of bubble radius and void fraction distribution for various stand-off distances. Reprint from [67], with permission from Elsevier, 2022, License Number 5830830883340.

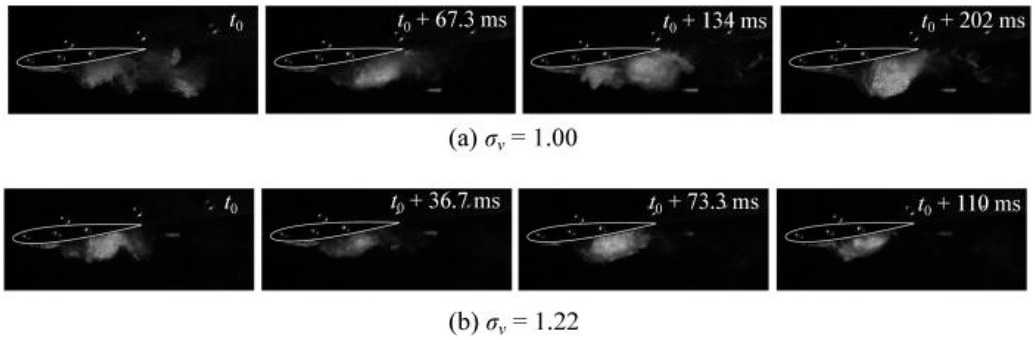


Figure 23. Snapshots of cloud cavitation in four successive shedding cycles. Reprint from [68] with permission from AIP Publishing, 2023, License Number 5830840703844.

Throughout the research above, a recurring theme is the intricate dance of forces and dynamics governing cloud bubble behavior in the vicinity of rigid boundaries. The collective insights from these studies furnish us with a comprehensive understanding of bubble cloud dynamics, from individual bubble behavior to collective cloud phenomena. Through experimental observations and sophisticated numerical simulations, a nuanced picture of bubble–wall interactions has emerged, laying the groundwork for future research and technological innovations in fields as diverse as ultrasonic cleaning, cavitation peening, and cavitation erosion prevention.

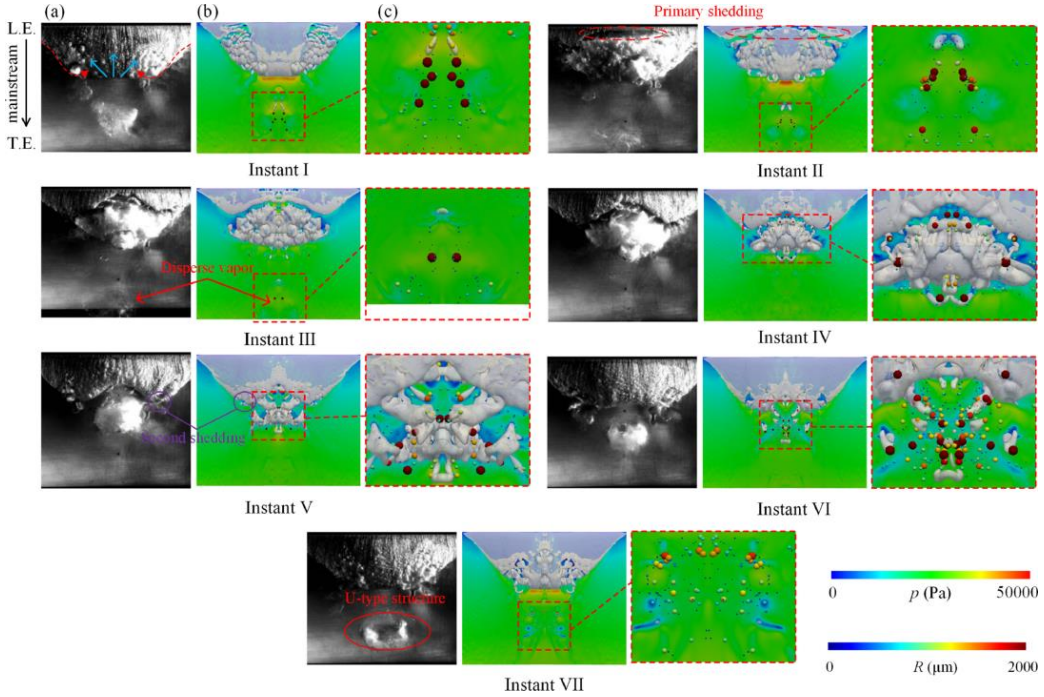


Figure 24. Observed and predicted time evolution of the multi-scale cavitating flow around the twisted hydrofoil: (**a**) experimental pictures, (**b**) global simulation results, and (**c**) partially enlarged simulation results. Reprint from [70], with permission from Elsevier, 2023, License Number 5830841056536.

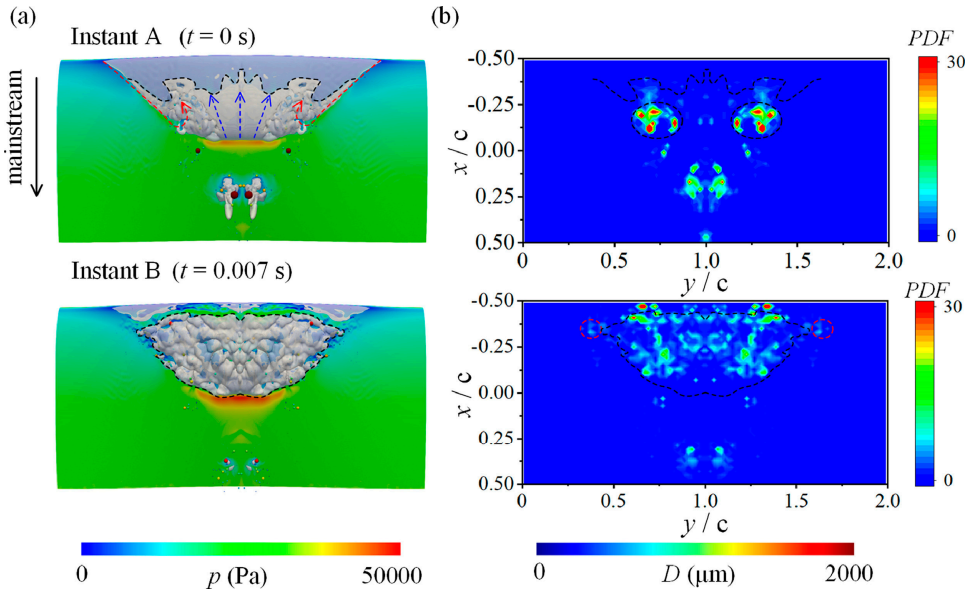


Figure 25. (**a**) Typical cavitating flow fields and (**b**) probability density of discrete bubble numbers at two typical instants during stage I. Reprint from [70], with permission from Elsevier, 2023, License Number 5830841056536.

4. Vortex Cavitation

In this section, we will discuss vortex bubbles' study in research that has applied numerical and experimental analyses combined with hydraulic machinery, mostly on tip vortices. A typical example of vortex cavitation is shown in Figure 26 [71].



Figure 26. Typical vortex cavitation [71].

In early work, tip vortex cavitation was observed [72]. Figure 27 shows the development of the tip and other forms of cavitation on a hydrofoil. By investigating the characteristics of cavitation near the tips of hydrofoils, valuable information such as Reynold's number and cavitation number was gathered to enhance our understanding of vortex cavitation's inception and development in practical hydrodynamic scenarios.

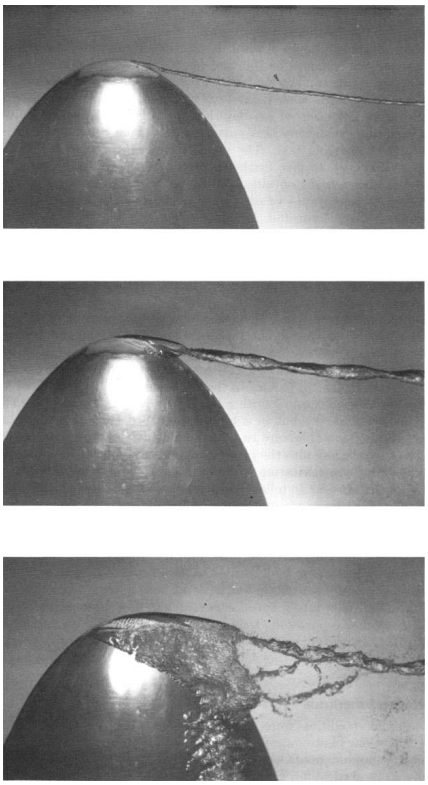


Figure 27. Photographs showing the development of a tip and other forms of cavitation on a hydrofoil, showing the continuous tip vortex cavity, tip vortex cavitation, secondary vortex cavitation, and surface cavitation. Reprint from [72], with permission from Cambridge University Press, 1991, License Number 5860660245448.

A study on the numerical simulation of three-dimensional cavitation shedding dynamics investigated the interaction between cavitation and vortices [73]. This study provides a comprehensive analysis of the formation and evolution of cavitation in vortical fluid flows. Through the mass transfer cavitation model and the modified RNG k-ε model, the shedding behavior of cavitation can be visualized through numerical analysis, as presented in Figure 28. Furthermore, Figure 29 shows the predicted vapor volume fraction and vorticity

contours for the middle plane during a typical cavity shedding cycle. Focusing on the dynamic interplay between cavitation bubbles and flow vortices, the study identified three types of flow behaviors along the suction side of the twisted hydrofoil, and demonstrated that cavitation promotes vortex production and increases the boundary layer thickness via local separation and flow unsteadiness. In sum, the numerical simulations presented in this study are noteworthy in capturing the intricate details of cavitation–vortex interactions, deepening our understanding of cavitation dynamics in three-dimensional flows.

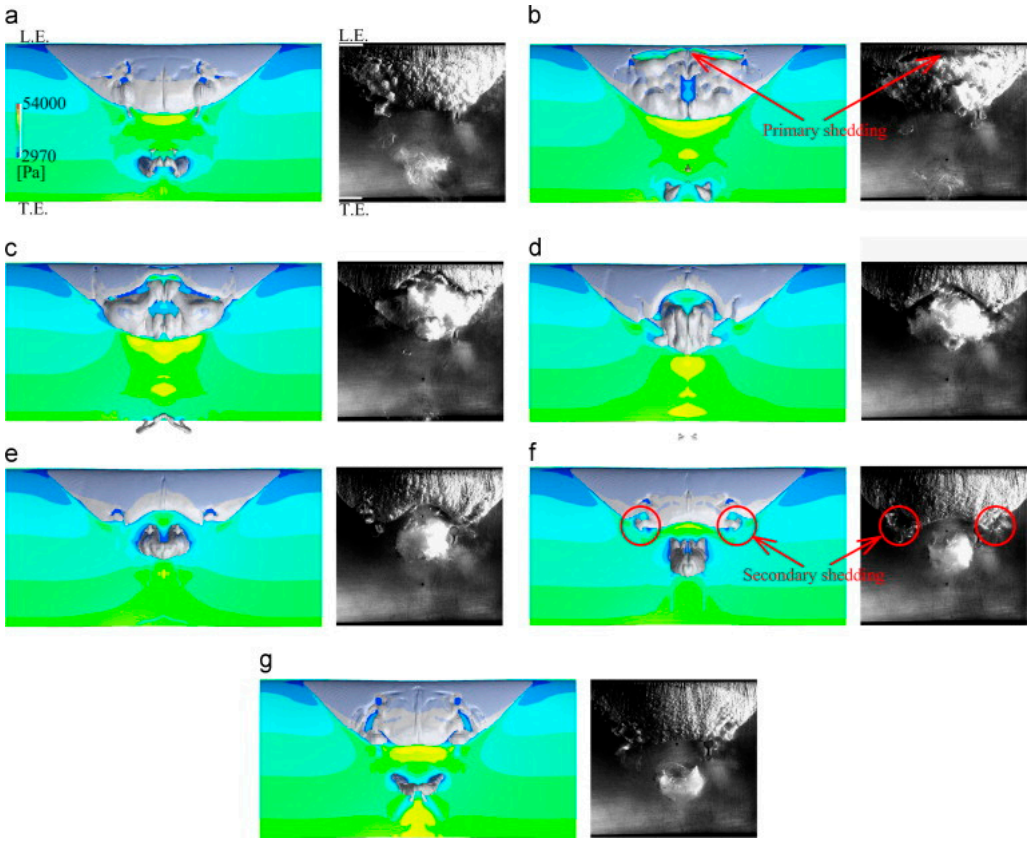


Figure 28. Top view of cavity shedding patterns for $\sigma = 1.07$ during one typical cycle (**a**–**g**). (Left: numerical results. Right: experimental observation by Foeth (2008) [74].) Reprint from [73] with permission from Elsevier, 2014, License Number 5830860095566.

The practical implications of cavitation in jet pump cavitation reactors (JPCRs) have also been explored via an investigation of the flow performance and induced noise [29]. The JPCR is an important object of study in vortex bubble research because it has great potential for future applications. Figure 30 shows its structure.

The important parameters of the JPCR are the flow ratio (q), pressure ratio (h), and efficiency (η), which are defined as follows:

$$q = \frac{Q_s}{Q_d} \tag{4}$$

$$h = \frac{P_0 - P_s}{P_d - P_s} = \frac{\left(\frac{p_0}{\rho_0 g} + \frac{{v_0}^2}{2g} + z_0\right) - \left(\frac{p_s}{\rho_s g} + \frac{{v_s}^2}{2g} + z_s\right)}{\left(\frac{p_d}{\rho_d g} + \frac{{v_d}^2}{2g} + z_0\right) - \left(\frac{p_s}{\rho_s g} + \frac{{v_s}^2}{2g} + z_s\right)} \tag{5}$$

$$\eta = \frac{\rho_s Q_S (P_0 - P_s)}{\rho_d Q_d (P_d - P_0)} = q\frac{h}{1-h} \tag{6}$$

where Q represents the flow rate, ρ the density, P the total pressure, p the hydrostatic pressure, z the elevation, and v the averaged flow velocity.

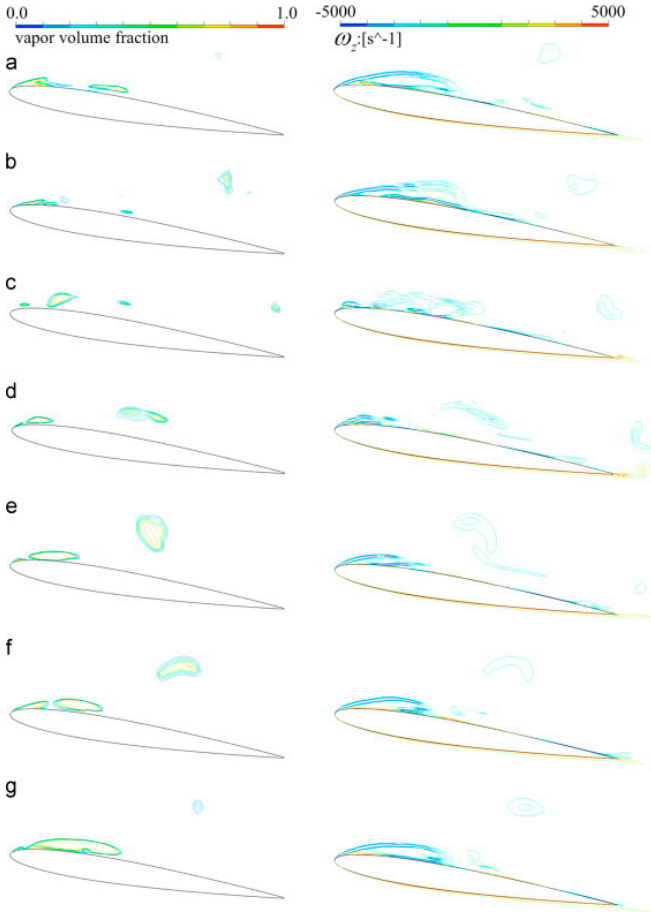


Figure 29. Comparison of vapor volume fraction (**left**) and vorticity (**right**) contours for $\sigma = 1.07$ at the plane with $z = 0$ during one typical cycle (**a**–**g**). Reprint from [73] with permission from Elsevier, 2014, License Number 5830860095566.

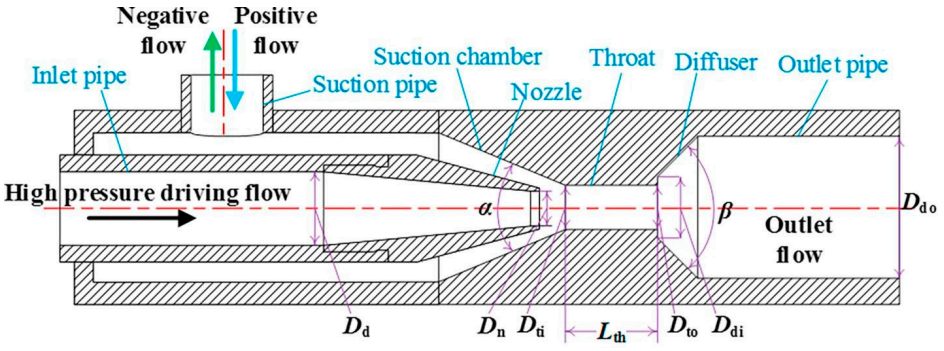


Figure 30. Schematic drawing of JPCR [29].

In Figure 31, we can see the vortex cavitation flow from the JPCR, and in Figure 32, we can see the various cavitation regions of JPCRs with different throat types. This team's research emphasizes the relationship between cavitation stages, noise signals, and flow parameters, which is helpful for JPCR design and application. The findings of their study, obtained by systematically altering the throat length, throat type, and diffuser angle, provide valuable insights into how we may optimize the design of cavitation reactors for various industrial processes, demonstrating that the JPCR has great potential as a piece of equipment for providing vortex cavitation.

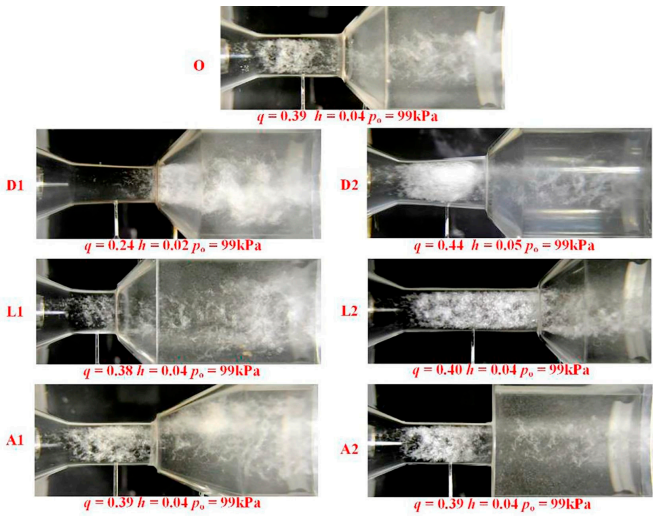


Figure 31. Typical cavitation images at the minimum outlet pressure for different JPCRs [29].

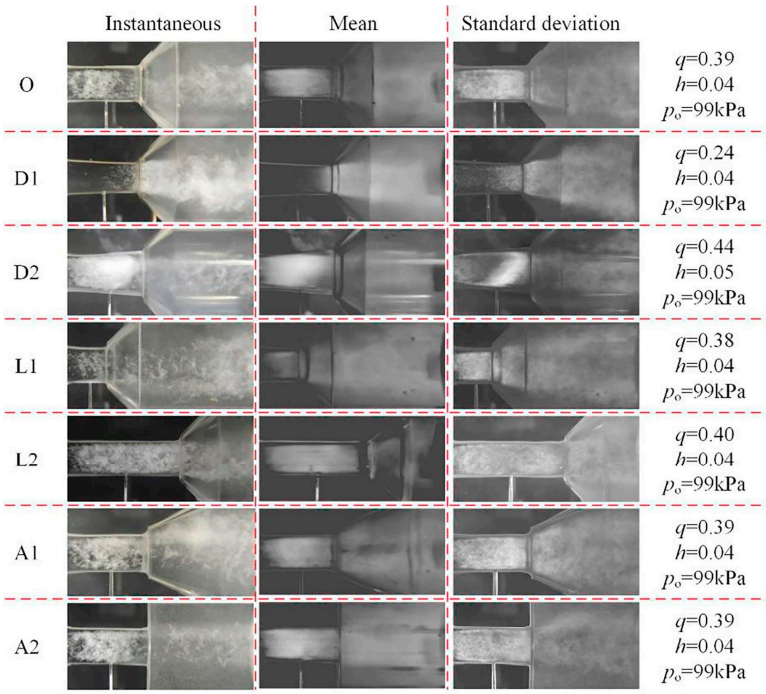


Figure 32. Typical cavitation images at the minimum outlet pressure for JPCRs with different structures [29].

In regard to the application of vortex cavitation, a noteworthy contribution has been made to our understanding of vortex generator effects on propeller cavitation and associated hull pressure fluctuations [75]. The findings of this experimental investigation underscored the role of vortex generators in mitigating the adverse effects caused by propeller cavitation. For instance, installing a vortex generator on a ship can improve sheet cavitation's stability and transparency when installed in the boundary layer and in front of the region of interest. Figure 33 shows cavitation with a vortex generator within a typical cycle. The vortex generator stabilizes cavitation and promotes energy transfer to a larger area on the hull surface. This dual impact of the vortex generator is a significant finding of the study, providing experimental insights into how adjustments in vortex generator configurations can potentially reduce cavitation impacts, offering an opportunity for the application of vortex bubble research.

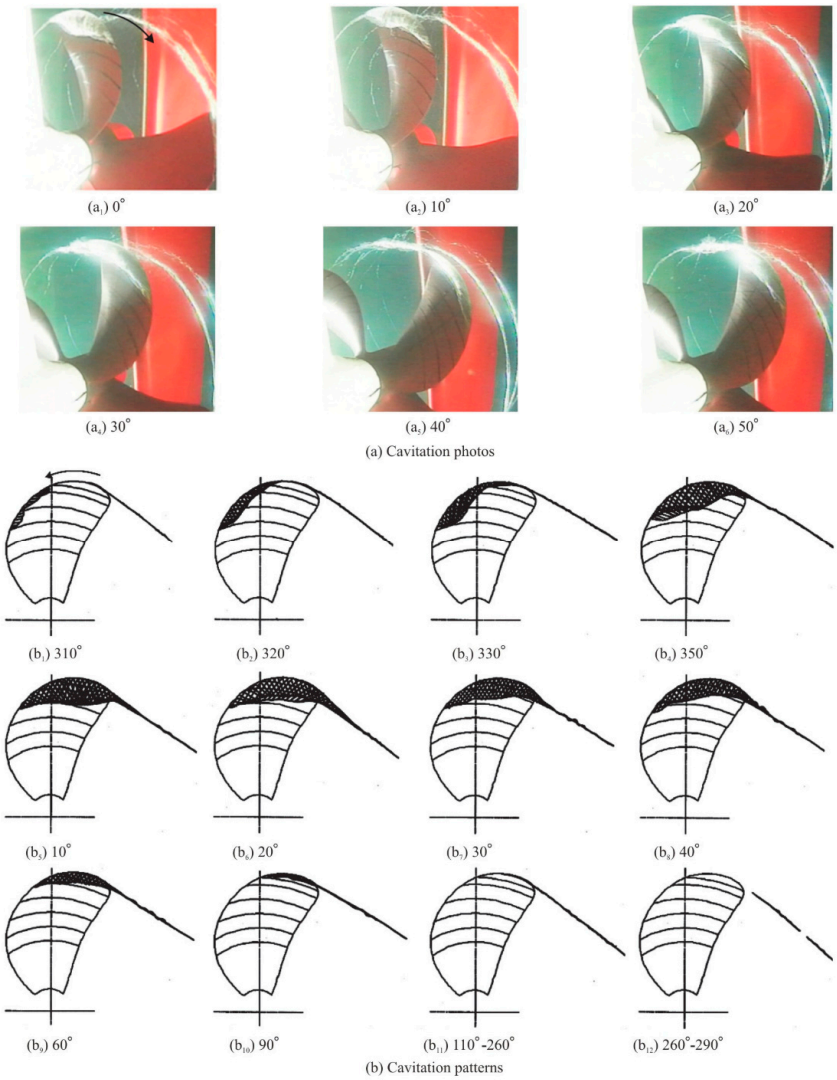


Figure 33. Measured cavitation results with a vortex generator within a typical cycle. Reprint from [75] with permission from Elsevier, 2020, License Number 5831390551079.

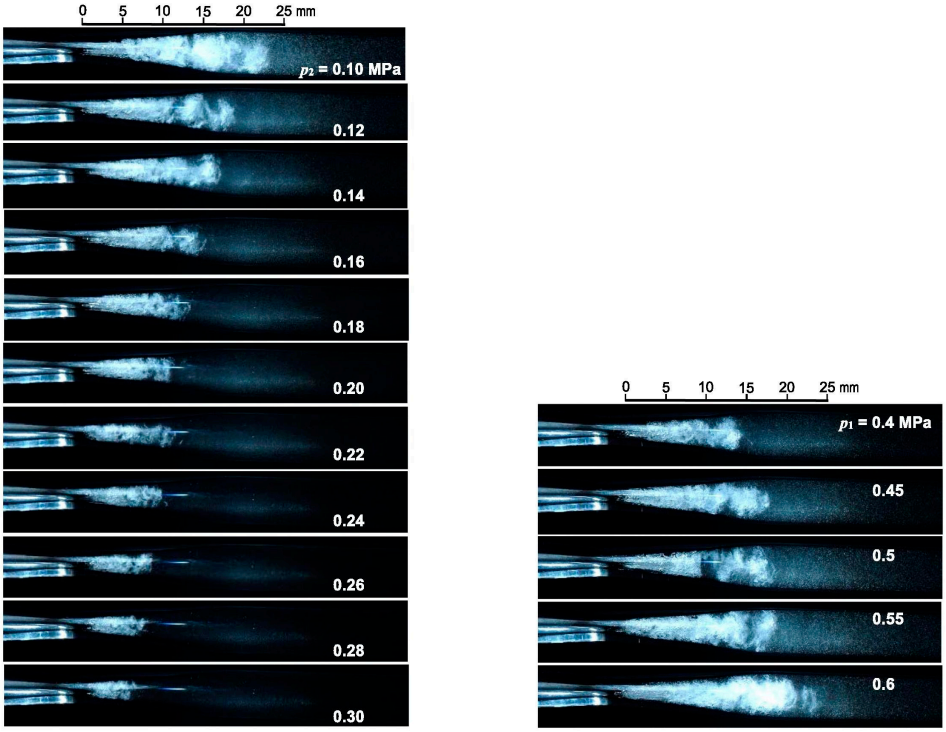
Similarly, another cavitation study focused on the acoustic pressures generated by laser-induced cavitation bubble expansion and collapse near rigid walls [76]. Their research revealed that the first and second shock waves released by cavitation bubbles have a depth relationship with γ, the distance ratio between the bubble's nucleation source, and its maximum size. Both pressure waves have the same amplitude for $\gamma = 2.5 \pm 0.1$ and $\gamma > 4$. The pressure and velocity in the numerical analysis also show a peak pressure generated during the bubble's collapse. Simulations predicted the behavior of the bubble, the bubble radius, and the formation and evolution of another vortex cavitation-like vortex. The study underscores the acoustic dimension of cavitation, which is closely related to the vortex bubbles' behavior when collapsing.

Advancing into the characteristics of vortex bubbles, a study applied high-speed photography to investigate the luminescence intensity of vortex cavitation within a Venturi tube and its variation with cavitation number [28]. The cavitation number was defined as follows:

$$\sigma = \frac{p_2 - p_v}{\frac{1}{2}\rho U^2} = \frac{p_2 - p_v}{p_1 - p_2} \tag{7}$$

where p_v and ρ are the vapor pressure and density of the test water, respectively, and U is the velocity at the throat.

As mentioned before, the Venturi tube structure is like that of a JPCR. In the Venturi tube, vortex cavitation can be observed clearly, as shown in Figures 34 and 35, which present the relationship between luminescence intensity and cavitation number. Here, the pressure wave was detected at the collapse of vortex cavitation. Moreover, the sound velocity was inflated, which was attributed to the aggressive intensity of the cavitation. This study explored cavitation's photonic emissions, and the researchers identified a crucial intersection between vortex bubbles and optical phenomena. This offers a new viewpoint on diagnosing and understanding cavitation's energy processes. Such work is integral to applications requiring the precise monitoring and control of cavitation to mitigate destructive effects or harness cavitation energy efficiently. The cited study set the foundation for future vortex bubble research in this regard.



(a) Aspects changing with downstream pressure p_2 (p_1 = 0.6 MPa) (b) Aspect changing with upstream pressure p_1 (p_2 = 0.1 MPa)

Figure 34. Typical aspects of cavitation in a Venturi tube: (**a**) aspects changing with downstream pressure p2 (p1 = 0.6 MPa); (**b**) aspect changing with upstream pressure p1 (p2 = 0.1 MPa) [28].

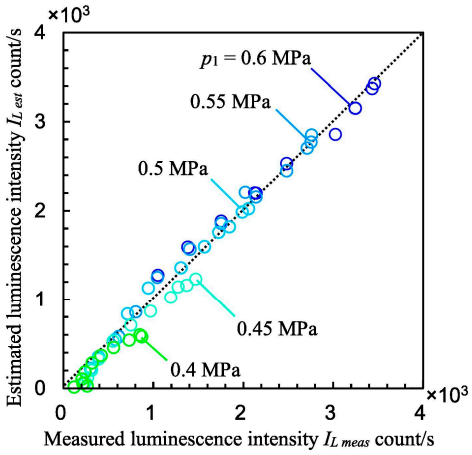


Figure 35. Relationship between measured luminescence intensity and estimated luminescence intensity [28].

A numerical and experimental study on vortex rings extended the discourse to the interaction between shock waves and vortex rings, which has implications for bubble collapse [77]. The vortex ring incubation corresponds to the shock wave when the bubble collapses, as shown in Figure 36. The intricacies of vortex dynamics revealed through this study are instrumental in comprehending how energy is transferred within fluid systems under the influence of shock waves, which directly relates to understanding bubble collapse and related pressure fluctuations.

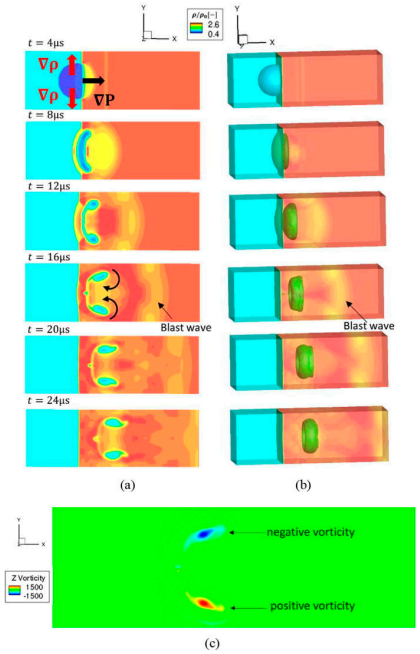


Figure 36. Numerical and experimental study on the behavior of vortex rings generated by shock–bubble interaction. (**a**) two–dimensional views; (**b**) three–dimensional views; (**c**) vorticity contours at t=16 μs. Reprint from [77], with permission from AIP Publishing, 2022, License Number 5831411280013.

A large eddy simulation study focusing on cloud cavitation and wake vortex cavitation around a trailing-truncated hydrofoil provided insights into their influence on the performance and safety of hydraulic machinery [78]. This study sheds light on the intricate flow structures associated with cavitation phenomena, revealing the interactions between cavitation bubbles and the surrounding flow field. The performance of cloud cavitation is shown in Figure 37. The characteristics of cloud bubbles and wake vortex bubbles can be observed. Through simulation, the researchers found that pressure-side bubbles were generally larger than suction-side bubbles in vortex cavitation, and their numerical analysis results matched their experimental results. In sum, these numerical and experimental analyses of cloud and vortex cavitation in hydrofoil machinery equipment help us understand the erosion mechanism at play.

In another large eddy simulation, the mechanisms of tip leakage vortex cavitation development in a cryogenic inducer were researched [79]. By analyzing thermodynamic effects and flow characteristics, this study uncovered how vortex cavitation instabilities, particularly with a tip leakage vortex, can be influenced and optimized in the design of cryogenic pumps. The numerical results agreed with the experimental results, proving that the numerical analysis was reliable. Tip leakage vortex cavitation is especially unstable due to the periodic coupling effect of cavity development, flow rate magnitude, and variation in local incidence angle due to the flow characteristics.

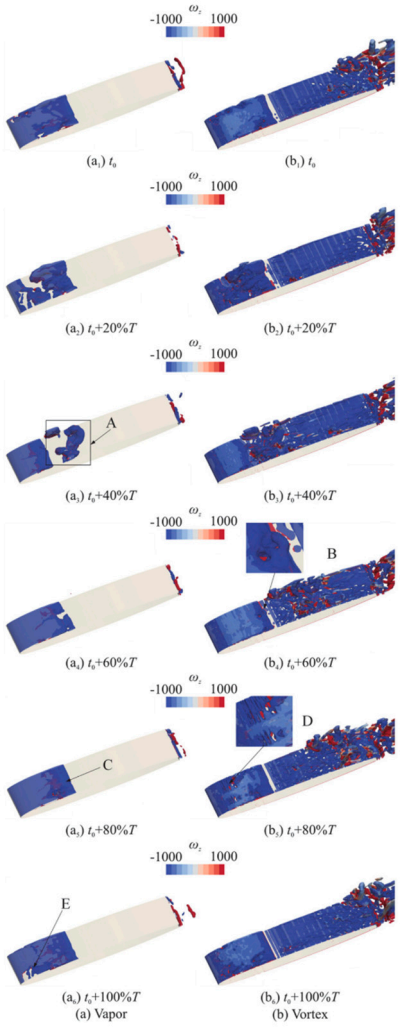


Figure 37. One-cycle shedding process of the cloud cavitation. A: horse-type cavity structure; B: small-scale U-type vortex; C: re-entrant jet; D: vortex tubes; E: non-uniform distribution of cavity and re-entrant jet. The cavity is visualized by the iso-surface with a vapor fraction of 0.1. All the structures are colored in terms of the spanwise vorticity component. Reprint from [78], with permission from Springer Nature, 2022, License Number 5831420313482.

In another area of bubble research, computer fluid dynamics in the Venturi tube have been explored through a numerical experimental analysis, where Eulerian–Lagrangian modeling was applied to the phase transition phenomena in cavitation-driven chemical processes [80]. Figure 38 shows the Venturi tube over time, reporting the axial velocity field with the 10% contour of the volume fraction overlapped. Figure 39 then shows the evolution of the bubbles for all the inlet pressures of 3 to 6 bar. The statistical results showed that the CFD code has an excellent predictive capability and can be used to assess the cavitation behavior in the Venturi tube compared to the experiment. By accurately predicting pressure peak values and bubble evolution using a multi-phase approach, the study demonstrates the efficacy of applying computer analyses in cavitation research. It also offers a reference on carrying out vortex bubble research in the Venturi tube, as well as the potential of cavitation technology in various chemical applications.

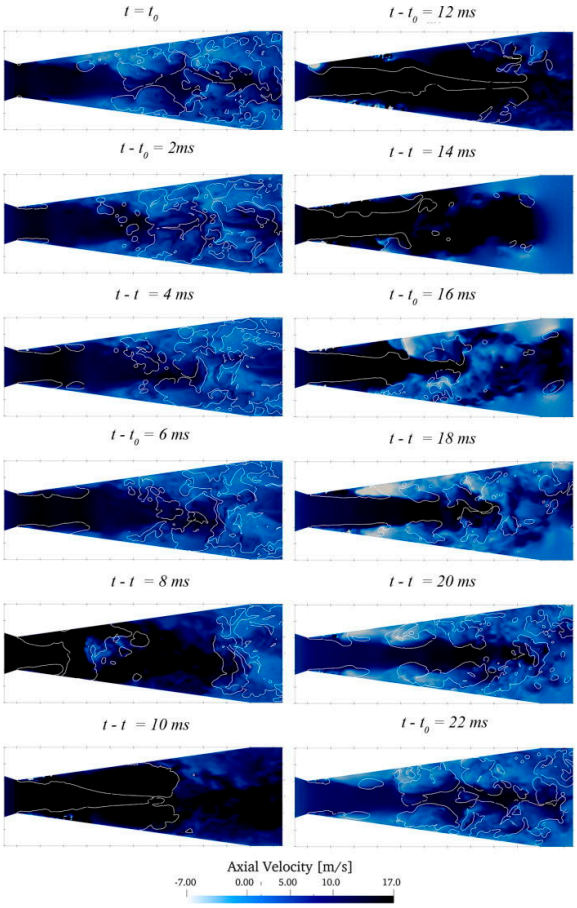


Figure 38. Cross-section of the velocity field with represented volume fraction contour $\gamma = 0.1$ [80].

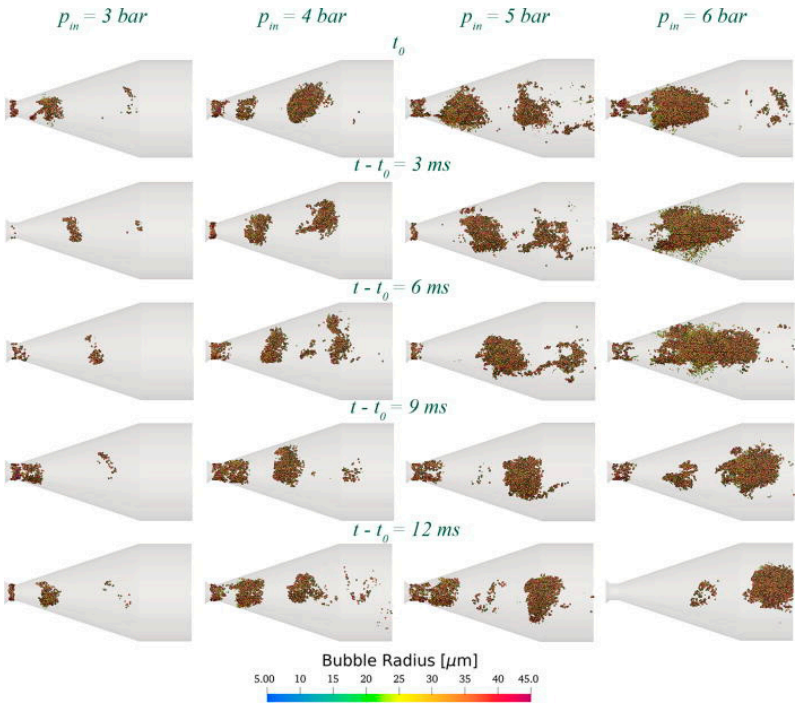
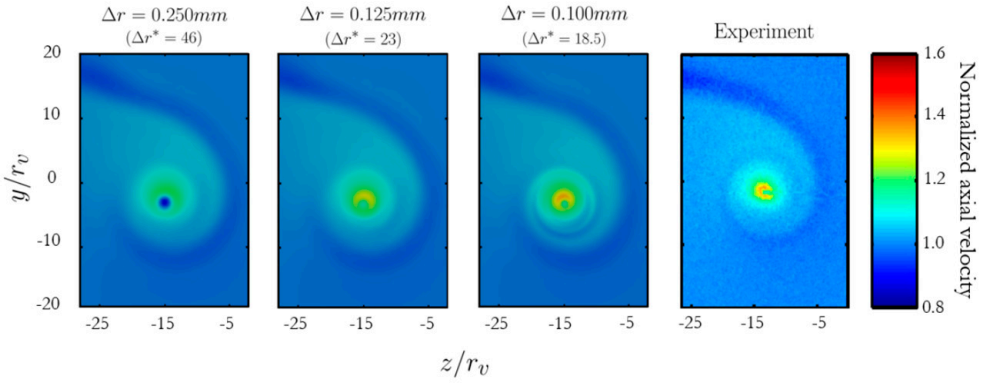


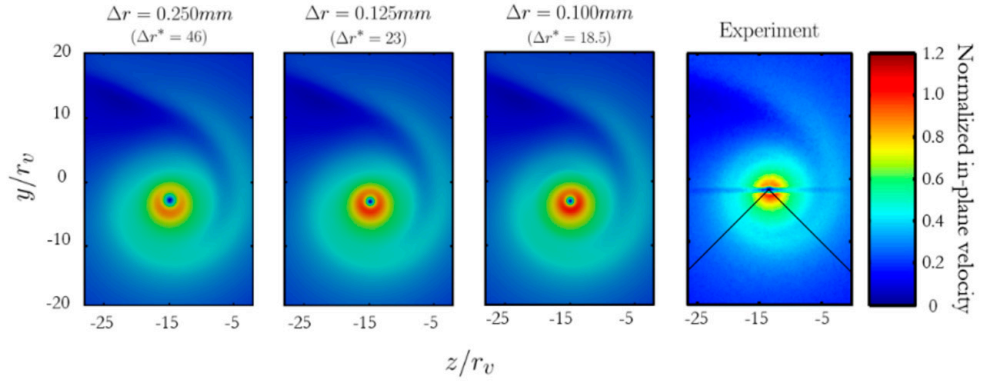
Figure 39. Bubble evolution for $p_{in} = 3$–6 bar [80].

Moreover, computer simulations were applied for a tip vortex, whereby a numerical investigation was performed of the oscillatory dynamics for different cavitation numbers,

focusing on an elliptical hydrofoil section [81]. This study used an effective radius based on the cross-sectional area of the tip vortex cavity, which captured cavity volume variations. Downstream, the study simulated the velocity distribution within the tip vortex region, as shown in Figure 40. Through the detailed simulations and analyses of cavity oscillations at varying cavitation numbers, the study revealed correlations between cavity dynamics, pressure fluctuations, and frequency shifts, contributing to our understanding of tip vortex cavitation behavior.



(a) Non-dimensional Axial Velocity



(b) Non-dimensional In-plane Velocity

Figure 40. Comparison of nondimensional velocity distribution within the tip vortex region at downstream location $x/c_0 = 1.14$, as obtained from simulations with different mesh sizes, with the experimental measurement [81].

Often, vortex bubbles are investigated through high-speed imaging, but bubbles have been characterized as spherical through numerical analysis. One option to overcome the limitations of these approaches is to instead apply X-ray imaging. Compared to visible light, X-ray imaging offers a different environment in which to observe vortex bubbles [55]. Figures 41 and 42 show the results of such imaging in a Venturi tube. There are many angulated bubbles as well as spherical bubbles, which should be considered when setting the assumptions in future numerical analyses. In addition, the tangential velocity of the surface of vortex cavitation is measured in this approach, along with the relationship of the geometry of the Venturi tube with the shedding frequency in vortex cavitation.

Previously, experimental investigations were performed on tip vortex cavitation (TVC) around a pitching hydrofoil in a cavitation tunnel [82–90]. The experiments used high-speed cameras, torque sensors, and hydrophones to analyze cavitation patterns, the torque exerted on the hydrofoil, and cavitation noise. These research studies focused on understanding the characteristics of TVC induced by the tip vortex and its impact under different flow conditions. After comparing and analyzing the phases of ascent, a static state, and descent, these studies concluded that the tip vortex cavitation intensity is the highest during the descent, moderate during the static state, and the lowest during the ascent.

In summary, the combination of extensive eddy simulations, multi-phase modeling, and advanced numerical techniques showcased in the above studies provides valuable insights into the complex phenomena of vortex cavitation, offering a comprehensive foundation for further research and engineering advancements in fluid dynamics and related fields.

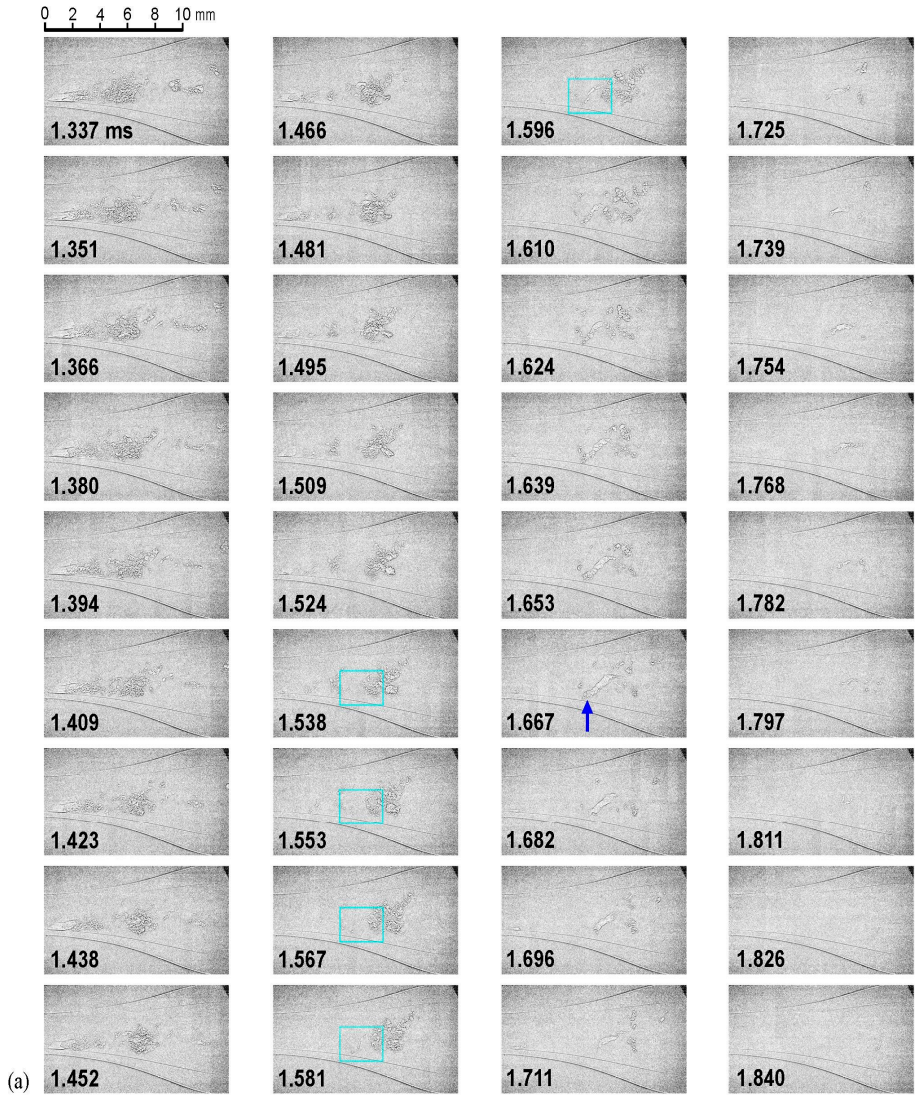


Figure 41. *Cont*.

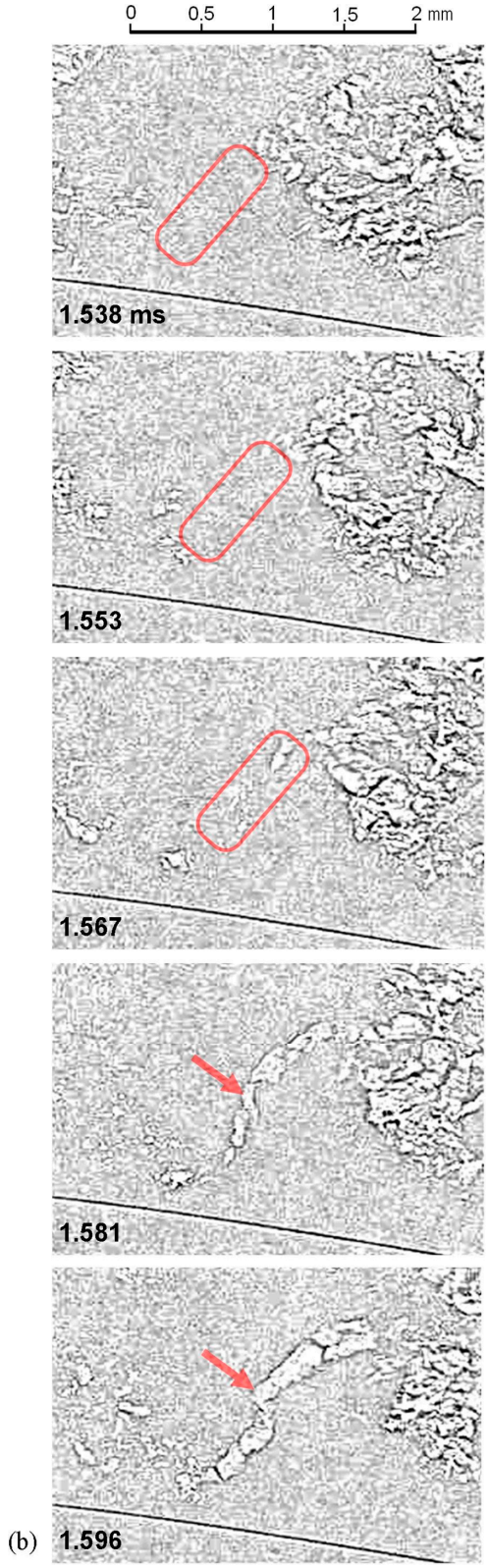


Figure 41. Vortex cavitation from shedding of trailing edge to collapse, observed by high-speed X-ray imaging. (**a**) Standard view of one cycle. (**b**) Magnified view [55].

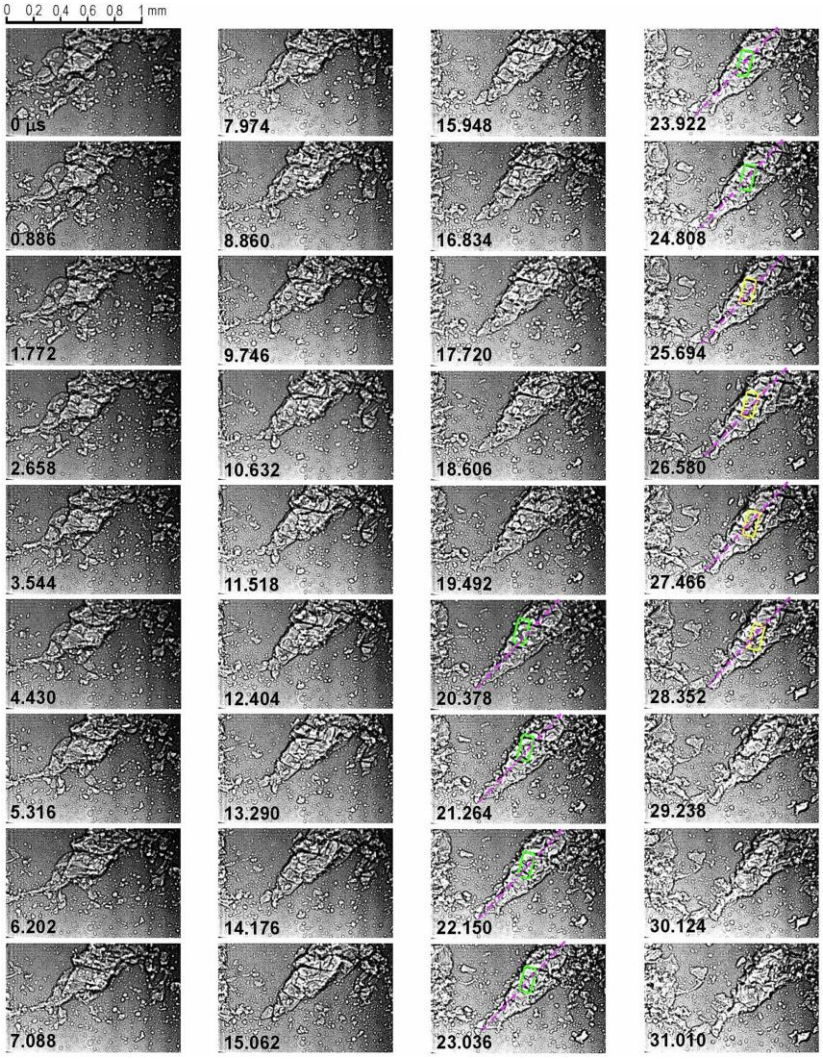


Figure 42. Rotation of vortex cavitation arising in the Venturi tube observed by XFEL [55].

5. Conclusions

This review has covered single cavitation bubbles, cloud cavitation bubbles, and vortex cavitation bubbles. Notably, most research on cavitation bubbles to date has concerned the mechanisms of bubble collapse near a solid boundary. Numerical analyses have been compared with experimental investigations, considering mass transfer, bubble shape, and so on. However, many areas remain to be explored in the research on bubbles, especially concerning their collapse mechanism. The key points highlighted in the present review can be summarized as follows:

(1) Cavitation peening is a new surface modification method used in the production of automobiles and stainless steel. It can improve the life of mechanical parts. However, cavitation bubbles near the solid boundary will cause erosion, such as in pumps and propellers. This highlights the importance of researching cavitation bubbles.

(2) The images obtained to date of cavitation bubbles and the trajectory of the cavitation bubble research field have been summarized, covering single cavitation bubbles, cloud cavitation bubbles, and vortex cavitation bubbles, with a focus on the images of cavitation bubbles near a solid boundary. An important finding is that many studies' numerical analyses of cavitation bubbles have pointed to them having the same characteristics as those depicted in the experimental images. However, recent research has brought to light an angular vortex cavitation bubble, as identified through X-ray imaging, which challenges our prior assumptions on the shapes of bubbles.

(3) The stand-off distance is a primary parameter impacting cavitation bubbles. Numerical and experimental analyses have proven that the stand-off distance is related to the stress and pressure caused by a bubble collapsing. Beyond that, this review has also introduced other parameters that are vital to incorporate when performing simulations, such as the cavitation number and governing equation.

Author Contributions: B.J.: conceptualization, methodology, and writing—original draft preparation. H.S.: visualization, supervision, and writing—review and editing. All authors have read and agreed to the published version of the manuscript.

Funding: This research was partly supported by JSPS KAKENHI (grant numbers 22KK0050 23K25988), JST CREST (JPMJCR2335), and the Suzuki Foundation (5-i19).

Data Availability Statement: The data presented in this study are available upon request from the authors.

Conflicts of Interest: The authors declare no conflicts of interest.

References

1. Soyama, H.; Tanaka, M.; Takiguchi, T.; Yamamoto, M. Development of a Cavitation Generator Mimicking Pistol Shrimp. *Biomimetics* **2024**, *9*, 47. [CrossRef] [PubMed]
2. Lohse, D.; Schmitz, B.; Versluis, M. Snapping shrimp make flashing bubbles. *Nature* **2001**, *413*, 477–478. [CrossRef] [PubMed]
3. Lillis, A.; Perelman, J.N.; Panyi, A.; Aran Mooney, T. Sound production patterns of big-clawed snapping shrimp (*Alpheus* spp.) are influenced by time-of-day and social context. *J. Acoust. Soc. Am.* **2017**, *142*, 3311–3320. [CrossRef] [PubMed]
4. Yang, Y.; Qin, S.; Di, C.; Qin, J.; Wu, D.; Zhao, J. Research on claw motion characteristics and cavitation bubbles of snapping shrimp. *Appl. Bionics Biomech.* **2020**, *2020*, 6585729. [CrossRef]
5. Larsen, O.N.; Reichmuth, C. Walruses produce intense impulse sounds by clap-induced cavitation during breeding displays. *R. Soc. Open Sci.* **2021**, *8*, 210197. [CrossRef]
6. Song, Z.; Salas, A.K.; Montie, E.W.; Laferriere, A.; Zhang, Y.; Aran Mooney, T. Sound pressure and particle motion components of the snaps produced by two snapping shrimp species (Alpheus heterochaelis and Alpheus angulosus). *J. Acoust. Soc. Am.* **2021**, *150*, 3288–3301. [CrossRef]
7. Kingston, A.C.N.; Woodin, S.A.; Wethey, D.S.; Speiser, D.I. Snapping shrimp have helmets that protect their brains by dampening shock waves. *Curr. Biol.* **2022**, *32*, 3576–3583.e3573. [CrossRef]
8. Dinh, J.P.; Patek, S.N. Weapon performance and contest assessment strategies of the cavitating snaps in snapping shrimp. *Funct. Ecol.* **2023**, *37*, 327–342. [CrossRef]
9. Versluis, M.; Schmitz, B.; von der Heydt, A.; Lohse, D. How Snapping Shrimp Snap: Through Cavitating Bubbles. *Science* **2000**, *289*, 2114–2117. [CrossRef]
10. Naude´, C.F.; Ellis, A.T. On the Mechanism of Cavitation Damage by Nonhemispherical Cavities Collapsing in Contact With a Solid Boundary. *J. Basic Eng.* **1961**, *83*, 648–656. [CrossRef]
11. Philipp, A.; Lauterborn, W. Cavitation erosion by single laser-produced bubbles. *J. Fluid Mech.* **1998**, *361*, 75–116. [CrossRef]
12. Brennen, C.E. *Cavitation and Bubble Dynamics*; Cambridge University Press: Cambridge, UK, 2013; pp. 90–95.
13. Gągol, M.; Przyjazny, A.; Boczkaj, G. Wastewater treatment by means of advanced oxidation processes based on cavitation—A review. *Chem. Eng. J.* **2018**, *338*, 599–627. [CrossRef]
14. Zheng, H.; Zheng, Y.; Zhu, J. Recent Developments in Hydrodynamic Cavitation Reactors: Cavitation Mechanism, Reactor Design, and Applications. *Engineering* **2022**, *19*, 180–198. [CrossRef]
15. Bagal, M.V.; Gogate, P.R. Wastewater treatment using hybrid treatment schemes based on cavitation and Fenton chemistry: A review. *Ultrason. Sonochemistry* **2014**, *21*, 1–14. [CrossRef]
16. Wang, B.; Liu, Y.; Zhang, H.; Shi, W.; Xiong, M.; Gao, C.; Cui, M. Hydrodynamic cavitation and its application in water treatment combined with ozonation: A review. *J. Ind. Eng. Chem.* **2022**, *114*, 33–51. [CrossRef]
17. Chen, Y.; Yin, C.; Song, Y. Application of hydrodynamic cavitation in the field of water treatment. *Chem. Pap.* **2023**, *77*, 3521–3546. [CrossRef]
18. Gogate, P.R.; Kabadi, A.M. A review of applications of cavitation in biochemical engineering/biotechnology. *Biochem. Eng. J.* **2009**, *44*, 60–72. [CrossRef]
19. Kelkar, M.A.; Gogate, P.R.; Pandit, A.B. Intensification of esterification of acids for synthesis of biodiesel using acoustic and hydrodynamic cavitation. *Ultrason. Sonochemistry* **2008**, *15*, 188–194. [CrossRef] [PubMed]
20. Innocenzi, V.; Prisciandaro, M. Technical feasibility of biodiesel production from virgin oil and waste cooking oil: Comparison between traditional and innovative process based on hydrodynamic cavitation. *Waste Manag.* **2021**, *122*, 15–25. [CrossRef]
21. Ahmad, A.; Yadav, A.K.; Singh, A.; Pal, A. Optimization of cavitation-assisted biodiesel production and fuel properties from Neochloris oleoabundans microalgae oil using genetic algorithm and response surface methodology. *Proc. Inst. Mech. Eng. Part E J. Process Mech. Eng.* **2024**, *238*, 1821–1835. [CrossRef]

22. Giuliano, A.; Cellamare, C.M.; Chiarini, L.; Tabacchioni, S.; Petta, L. Evaluation of the controlled hydrodynamic cavitation as gas mass transfer system for ex-situ biological hydrogen methanation. *Chem. Eng. J.* **2023**, *471*, 144475. [CrossRef]
23. Deggelmann, M.; Nöpel, J.-A.; Rüdiger, F.; Paustian, D.; Braeutigam, P. Hydrodynamic cavitation for micropollutant degradation in water—Correlation of bisphenol A degradation with fluid mechanical properties. *Ultrason. Sonochemistry* **2022**, *83*, 105950. [CrossRef]
24. Agarkoti, C.; Gujar, S.K.; Gogate, P.R.; Pandit, A.B. Pilot scale degradation of Sulfamerazine using different venturi based hydrodynamic cavitation and ultrasound reactors in combination with oxidation processes. *J. Environ. Chem. Eng.* **2023**, *11*, 109857. [CrossRef]
25. Feng, Z.; Wang, F.; Zhu, K.; Wang, Z.; Ning, J. Degradation of ammonia nitrogen by an economic combined hydrodynamic cavitation method. *Environ. Sci. Pollut. Res.* **2023**, *30*, 72782–72792. [CrossRef]
26. Min Oo, Y.; Somnuk, K. Investigation of free fatty acid reduction from mixed crude palm oil using 3D-printed rotor–stator hydrodynamic cavitation: An experimental study of geometric characteristics of the inner hole. *Ultrason. Sonochemistry* **2023**, *98*, 106472. [CrossRef] [PubMed]
27. Xu, S.; Wang, J.; Chen, W.; Ji, B.; Yan, H.; Zhang, Z.; Long, X. Removal of field-collected Microcystis aeruginosa in pilot-scale by a jet pump cavitation reactor. *Ultrason. Sonochemistry* **2022**, *83*, 105924. [CrossRef] [PubMed]
28. Soyama, H. Luminescence intensity of vortex cavitation in a venturi tube changing with cavitation number. *Ultrason. Sonochemistry* **2021**, *71*, 105389. [CrossRef] [PubMed]
29. Wang, J.; Cheng, H.; Xu, S.; Ji, B.; Long, X. Performance of cavitation flow and its induced noise of different jet pump cavitation reactors. *Ultrason. Sonochemistry* **2019**, *55*, 322–331. [CrossRef]
30. Liu, L.; Yang, X.; Guo, Y.; Li, B.; Wang, L.-P. Reactive mixing performance for a nanoparticle precipitation in a swirling vortex flow reactor. *Ultrason. Sonochemistry* **2023**, *94*, 106332. [CrossRef]
31. Song, Y.; Hou, R.; Liu, Z.; Liu, J.; Zhang, W.; Zhang, L. Cavitation characteristics analysis of a novel rotor-radial groove hydrodynamic cavitation reactor. *Ultrason. Sonochemistry* **2022**, *86*, 106028. [CrossRef]
32. Soyama, H.; Korsunsky, A.M. A critical comparative review of cavitation peening and other surface peening methods. *J. Mater. Process. Technol.* **2022**, *305*, 117586. [CrossRef]
33. Soyama, H. Improvement of Fatigue Strength of 3D-Metal by Combined Process of Blasting and Cavitation Peening. In Proceedings of the 3rd International Conference on Advanced Surface Enhancement (INCASE) 2023, Singapore, 25–27 September 2023.
34. Soyama, H.; Shimizu, M.; Hattori, Y.; Nagasawa, Y. Improving the fatigue strength of the elements of a steel belt for CVT by cavitation shotless peening. *J. Mater. Sci.* **2008**, *43*, 5028–5030. [CrossRef]
35. Soyama, H.; Sekine, Y. Sustainable surface modification using cavitation impact for enhancing fatigue strength demonstrated by a power circulating-type gear tester. *Int. J. Sustain. Eng.* **2010**, *3*, 25–32. [CrossRef]
36. Zhang, Y.; Zhang, Y.; Qian, Z.; Ji, B.; Wu, Y. A review of microscopic interactions between cavitation bubbles and particles in silt-laden flow. *Renew. Sustain. Energy Rev.* **2016**, *56*, 303–318. [CrossRef]
37. Wang, T.; Chen, L. Thermodynamic Behavior and Energy Transformation Mechanism of the Multi-Period Evolution of Cavitation Bubbles Collapsing near a Rigid Wall: A Numerical Study. *Energies* **2023**, *16*, 1048. [CrossRef]
38. Yu, J.; Yan, J.; Jiang, L.; Li, J.; Guo, H.; Qiao, M.; Qu, L. Fluorescence enhancement of organic dyes by femtosecond laser-induced cavitation bubbles for crystal imaging. *Nanoscale* **2023**, *15*, 8730–8739. [CrossRef] [PubMed]
39. Subramanian, R.K.; Coutier-Delgosha, O. Intrusive temperature measurement of the cavitation bubbles using cold wire. *J. Acoust. Soc. Am.* **2022**, *152*, A249. [CrossRef]
40. Reuter, F.; Cairós, C.; Mettin, R. Vortex dynamics of collapsing bubbles: Impact on the boundary layer measured by chronoamperometry. *Ultrason. Sonochemistry* **2016**, *33*, 170–181. [CrossRef]
41. Yasui, K. Production of O Radicals from Cavitation Bubbles under Ultrasound. *Molecules* **2022**, *27*, 4788. [CrossRef]
42. Izak Ghasemian, S.; Reuter, F.; Ohl, C.D. High-speed ultrasound imaging of laser-induced cavitation bubbles. *Appl. Phys. Lett.* **2021**, *119*, 114101. [CrossRef]
43. Krella, A.K. Degradation and Protection of Materials from Cavitation Erosion: A Review. *Materials* **2023**, *16*, 2058. [CrossRef] [PubMed]
44. Reuter, F.; Gonzalez-Avila, S.R.; Mettin, R.; Ohl, C.-D. Flow fields and vortex dynamics of bubbles collapsing near a solid boundary. *Phys. Rev. Fluids* **2017**, *2*, 064202. [CrossRef]
45. Iga, Y.; Sasaki, H. Relationship between a non-spherical collapse of a bubble and a stress state inside a wall. *Phys. Fluids* **2023**, *35*, 023312. [CrossRef]
46. Vogel, A.; Lauterborn, W. Acoustic transient generation by laser-produced cavitation bubbles near solid boundaries. *J. Acoust. Soc. Am.* **1988**, *84*, 719–731. [CrossRef]
47. Hickling, R.; Plesset, M.S. Collapse and Rebound of a Spherical Bubble in Water. *Phys. Fluids* **1964**, *7*, 7–14. [CrossRef]
48. Benjamin, T.B.; Ellis, A.T. The Collapse of Cavitation Bubbles and the Pressures thereby Produced against Solid Boundaries. *Philos. Trans. R. Soc. London. Ser. A Math. Phys. Sci.* **1966**, *260*, 221–240.
49. Chapman, R.B.; Plesset, M.S. Collapse of an initially spherical vapour cavity in the neighbourhood of a solid boundary. *J. Fluid Mech.* **1971**, *47*, 283–290.

50. Brujan, E.; Keen, G.; Vogel, A.; Blake, J. The final stage of the collapse of a cavitation bubble close to a rigid boundary. *Phys. Fluids* **2002**, *14*, 85–92. [CrossRef]
51. Brujan, E.A.; Ikeda, T.; Yoshinaka, K.; Matsumoto, Y. The final stage of the collapse of a cloud of bubbles close to a rigid boundary. *Ultrason. Sonochemistry* **2011**, *18*, 59–64. [CrossRef]
52. Colonius, T.I.M.; Johnsen, E. Numerical simulations of non-spherical bubble collapse. *J. Fluid Mech.* **2009**, *629*, 231–262.
53. Li, S.; Zhang, A.M.; Han, R.; Liu, Y. Experimental and numerical study on bubble-sphere interaction near a rigid wall. *Phys. Fluids* **2017**, *29*, 092102. [CrossRef]
54. Fujikawa, S.; Akamatsu, T. Experimental Investigations of Cavitation Bubble Collapse by a Water Shock Tube. *Bull. JSME* **1978**, *21*, 223–230. [CrossRef]
55. Soyama, H.; Liang, X.; Yashiro, W.; Kajiwara, K.; Asimakopoulou, E.M.; Bellucci, V.; Birnsteinova, S.; Giovanetti, G.; Kim, C.; Kirkwood, H.J.; et al. Revealing the origins of vortex cavitation in a Venturi tube by high speed X-ray imaging. *Ultrason. Sonochemistry* **2023**, *101*, 106715. [CrossRef]
56. Soyama, H.; Iga, Y. Laser Cavitation Peening: A Review. *Appl. Sci.* **2023**, *13*, 6702. [CrossRef]
57. Soyama, H. Development of Laser Cavitation Peening Using a Normal-Oscillation Nd:YAG Laser. *Coatings* **2023**, *13*, 1395. [CrossRef]
58. Kuji, C.; Soyama, H. Mechanical Surface Treatment of Titanium Alloy Ti6Al4V Manufactured by Direct Metal Laser Sintering Using Laser Cavitation. *Metals* **2023**, *13*, 181. [CrossRef]
59. Soyama, H.; Kuji, C.; Liao, Y. Comparison of the effects of submerged laser peening, cavitation peening and shot peening on the improvement of the fatigue strength of magnesium alloy AZ31. *J. Magnes. Alloys* **2023**, *11*, 1592–1607. [CrossRef]
60. Sasaki, H.; Ochiai, N.; Iga, Y. Numerical Analysis of Damping Effect of Liquid Film on Material in High Speed Liquid Droplet Impingement. *Int. J. Fluid Mach. Syst.* **2016**, *9*, 57–65. [CrossRef]
61. Aganin, A.A.; Davletshin, A.I. A particle model of interaction between weakly non-spherical bubbles. *Appl. Math. Model.* **2024**, *126*, 185–205. [CrossRef]
62. Chahine, G.L.; Duraiswami, R. Dynamical interactions in a multi-bubble cloud. *J. Fluids Eng.* **1992**, *114*, 680. [CrossRef]
63. Reisman, G.E.; Wang, Y.C.; Brennen, C.E. Observations of shock waves in cloud cavitation. *J. Fluid Mech.* **1998**, *355*, 255–283. [CrossRef]
64. Ma, J.; Hsiao, C.-T.; Chahine, G.L. Euler–Lagrange Simulations of Bubble Cloud Dynamics Near a Wall. *J. Fluids Eng.* **2015**, *137*, 041301. [CrossRef]
65. Ma, J.; Hsiao, C.T.; Chahine, G.L. Dynamics of a Bubble Cloud near a Rigid Wall. *J. Phys. Conf. Ser.* **2015**, *656*, 012153. [CrossRef]
66. Ma, J.; Hsiao, C.-T.; Chahine, G.L. Numerical study of acoustically driven bubble cloud dynamics near a rigid wall. *Ultrason. Sonochemistry* **2018**, *40*, 944–954. [CrossRef] [PubMed]
67. Okita, K.; Miyamoto, Y.; Furukawa, T.; Takagi, S. Numerical study on stress in a solid wall caused by the collapse of a cavitation bubble cloud in hydraulic fluid. *Int. J. Multiph. Flow* **2022**, *150*, 103965. [CrossRef]
68. Liu, Y.; Zhang, H.; Zhang, W.; Wang, B. Bubble Size Distribution at Early Stage of Hydrodynamic Cloud Cavitation. *SSRN Electron. J.* **2023**, *35*, 063305. [CrossRef]
69. Zhang, H.; Liu, Y.; Wang, B. Spatial-temporal features of the coherent structure of sheet/cloud cavitation flows using a frequency-weighted dynamic mode decomposition approach. *Phys. Fluids* **2021**, *33*, 053317. [CrossRef]
70. Wang, Z.; Cheng, H.; Ji, B.; Peng, X. Numerical investigation of inner structure and its formation mechanism of cloud cavitating flow. *Int. J. Multiph. Flow* **2023**, *165*, 104484. [CrossRef]
71. Soyama, H.; Ohba, K.; Takeda, S.; Oba, R. High-speed observations of highly erosive vortex cavitation around butterfly valve. *JSME* **1994**, *60*, 1133–1138. [CrossRef]
72. Arndt, R.; Arakeri, V.; Higuchi, H. Some observations of tip-vortex cavitation. *J. Fluid Mech.* **1991**, *229*, 269–289. [CrossRef]
73. Ji, B.; Luo, X.; Arndt, R.E.; Wu, Y. Numerical simulation of three dimensional cavitation shedding dynamics with special emphasis on cavitation–vortex interaction. *Ocean Eng.* **2014**, *87*, 64–77. [CrossRef]
74. Foeth, E.-J.; van Terwisga, T.; van Doorne, C. On the Collapse Structure of an Attached Cavity on a Three-Dimensional Hydrofoil. *J. Fluids Eng.* **2008**, *130*, 071303. [CrossRef]
75. Huang, H.-b.; Long, Y.; Ji, B. Experimental investigation of vortex generator influences on propeller cavitation and hull pressure fluctuations. *J. Hydrodyn.* **2020**, *32*, 82–92. [CrossRef]
76. Gonzalez-Avila, S.R.; Denner, F.; Ohl, C.-D. The acoustic pressure generated by the cavitation bubble expansion and collapse near a rigid wall. *Phys. Fluids* **2021**, *33*, 032118. [CrossRef]
77. Kitamura, K.; Yue, Z.; Fujimoto, T.; Asai, H.; Kubota, A.; Myokan, M.; Ichihara, D.; Sasoh, A. Numerical and experimental study on the behavior of vortex rings generated by shock–bubble interaction. *Phys. Fluids* **2022**, *34*, 046105. [CrossRef]
78. Yin, T.; Pavesi, G.; Pei, J.; Yuan, S.Q.; Gan, X. Large eddy simulation of cloud cavitation and wake vortex cavitation around a trailing-truncated hydrofoil. *J. Hydrodyn.* **2022**, *34*, 893–903. [CrossRef]
79. Chen, T.; Mu, Z.; Chen, J.; Tan, S.; Fan, Y. Numerical investigations on the mechanisms of the tip leakage vortex cavitation development in a cryogenic inducer with large eddy simulation. *Phys. Fluids* **2023**, *35*, 073328. [CrossRef]
80. Duronio, F.; Di Mascio, A.; De Vita, A.; Innocenzi, V.; Prisciandaro, M. Eulerian–Lagrangian modeling of phase transition for application to cavitation-driven chemical processes. *Phys. Fluids* **2023**, *35*, 053305. [CrossRef]
81. Lak, S.; Jaiman, R. A numerical study on the oscillatory dynamics of tip vortex cavitation. *arXiv* **2023**, arXiv:2312.15579.

82. Wang, L.; Wang, P.; Wu, K.; Wang, H.; Huang, B.; Wu, D. Experiment investigation of the tip vortex cavitation around a pitching hydrofoil. *Phys. Fluids* **2023**, *35*, 103313. [CrossRef]
83. Amini, A.; Reclari, M.; Sano, T.; Iino, M.; Farhat, M. Suppressing tip vortex cavitation by winglets. *Exp. Fluids* **2019**, *60*, 159. [CrossRef]
84. Chahine, G.L.; Hsiao, C.-T.; Raju, R. Scaling of cavitation bubble cloud dynamics on propellers. In *Advanced Experimental and Numerical Techniques for Cavitation Erosion Prediction. Fluid Mechanics and Its Applications*; Springer: Dordrecht, The Netherlands, 2014; Volume 106; pp. 345–372.
85. Khoo, M.T.; Venning, J.A.; Pearce, B.W.; Brandner, P.A. Nucleation and cavitation number effects on tip vortex cavitation dynamics and noise. *Exp. Fluids* **2021**, *62*, 216. [CrossRef]
86. Lee, J.-H.; Han, J.-M.; Park, H.-G.; Seo, J.-S. Application of signal processing techniques to the detection of tip vortex cavitation noise in marine propeller. *J. Hydrodyn.* **2013**, *25*, 440–449. [CrossRef]
87. Park, I.; Kim, J.; Paik, B.; Seol, H. Numerical Study on Tip Vortex Cavitation Inception on a Foil. *Appl. Sci.* **2021**, *11*, 7332. [CrossRef]
88. Park, K.; Seol, H.; Choi, W.; Lee, S. Numerical prediction of tip vortex cavitation behavior and noise considering nuclei size and distribution. *Appl. Acoust.* **2009**, *70*, 674–680. [CrossRef]
89. Peng, X.-X.; Zhang, L.-X.; Wang, B.-L.; Xu, L.-H.; Song, M.-T.; Cao, Y.-T.; Liu, Y.-W.; Hong, F.-W.; Yan, K. Study of tip vortex cavitation inception and vortex singing. *J. Hydrodyn.* **2019**, *31*, 1170–1177. [CrossRef]
90. Zhang, L.-X.; Zhang, N.; Peng, X.-X.; Wang, B.-L.; Shao, X.-M. A review of studies of mechanism and prediction of tip vortex cavitation inception. *J. Hydrodyn.* **2015**, *27*, 488–495. [CrossRef]

Disclaimer/Publisher's Note: The statements, opinions and data contained in all publications are solely those of the individual author(s) and contributor(s) and not of MDPI and/or the editor(s). MDPI and/or the editor(s) disclaim responsibility for any injury to people or property resulting from any ideas, methods, instructions or products referred to in the content.